Stem Cell Reports
Article

ISSCR

OPEN ACCESS

The blood-brain barrier is dysregulated in COVID-19 and serves as a CNS entry route for SARS-CoV-2

Susanne Krasemann,[1,2,*] Undine Haferkamp,[3,19,21] Susanne Pfefferle,[4,5,6,21] Marcel S. Woo,[7] Fabian Heinrich,[8] Michaela Schweizer,[9] Antje Appelt-Menzel,[10,11] Alevtina Cubukova,[11] Janica Barenberg,[3,19] Jennifer Leu,[3,19] Kristin Hartmann,[1,2] Edda Thies,[1] Jessica Lisa Littau,[1] Diego Sepulveda-Falla,[1] Liang Zhang,[12] Kathy Ton,[12] Yan Liang,[12] Jakob Matschke,[1] Franz Ricklefs,[13] Thomas Sauvigny,[13] Jan Sperhake,[8] Antonia Fitzek,[8] Anna Gerhartl,[14] Andreas Brachner,[14] Nina Geiger,[20] Eva-Maria König,[20] Jochen Bodem,[20] Sören Franzenburg,[15] Andre Franke,[15] Stefan Moese,[16] Franz-Josef Müller,[17] Gerd Geisslinger,[18,19] Carsten Claussen,[3,19] Aimo Kannt,[18,19] Andrea Zaliani,[3,19] Philip Gribbon,[3,19] Benjamin Ondruschka,[8] Winfried Neuhaus,[14] Manuel A. Friese,[7] Markus Glatzel,[1] and Ole Pless[3,19,*]

[1]Institute for Neuropathology, University Medical Center Hamburg-Eppendorf, 20246 Hamburg, Germany
[2]Experimental Pathology Core Facility, University Medical Center Hamburg-Eppendorf, 20246 Hamburg, Germany
[3]Fraunhofer Institute for Translational Medicine and Pharmacology ITMP, Discovery Research ScreeningPort, 22525 Hamburg, Germany
[4]Institute for Medical Microbiology, Virology and Hygiene, University Medical Center Hamburg-Eppendorf, 20246 Hamburg, Germany
[5]Bernhard Nocht Institute, Leibniz Institute for Tropical Medicine, 20359 Hamburg, Germany
[6]German Center for Infection Research, Partner Site Hamburg-Borstel-Lübeck-Riems, 20359 Hamburg, Germany
[7]Institute of Neuroimmunology and Multiple Sclerosis, University Medical Center Hamburg-Eppendorf, 20251 Hamburg, Germany
[8]Institute of Legal Medicine, University Medical Center Hamburg-Eppendorf, 20246 Hamburg, Germany
[9]Morphology and Electron Microscopy Core Facility, Center for Molecular Neurobiology (ZMNH), University Medical Center Hamburg-Eppendorf, 20251 Hamburg, Germany
[10]University Hospital Würzburg, Chair Tissue Engineering and Regenerative Medicine (TERM), 97070 Würzburg, Germany
[11]Fraunhofer Institute for Silicate Research (ISC), Translational Center Regenerative Therapies (TLC-RT), 97070 Würzburg, Germany
[12]Nanostring Technologies, Seattle, WA 98109, USA
[13]Department for Neurosurgery, University Medical Center Hamburg-Eppendorf, 20246 Hamburg, Germany
[14]AIT-Austrian Institute of Technology GmbH, 1210 Wien, Austria
[15]Institute of Clinical Molecular Biology, Universitätsklinikum Schleswig-Holstein, 24105 Kiel, Germany
[16]Neurimmune AG, 8952 Schlieren, Switzerland
[17]Zentrum für Integrative Psychiatrie (ZIP) GmbH, Universitätsklinikum Schleswig-Holstein, 24105 Kiel, Germany
[18]Fraunhofer Institute for Translational Medicine and Pharmacology (ITMP), 60596 Frankfurt am Main, Germany
[19]Fraunhofer Cluster of Excellence for Immune-Mediated Diseases (CIMD), 60596 Frankfurt am Main, Germany
[20]University Würzburg, Institute of Virology and Immunobiology, 97078 Würzburg, Germany
[21]These authors contributed equally
*Correspondence: s.krasemann@uke.de (S.K.), ole.pless@itmp.fraunhofer.de (O.P.)
https://doi.org/10.1016/j.stemcr.2021.12.011

SUMMARY

Neurological complications are common in COVID-19. Although SARS-CoV-2 has been detected in patients' brain tissues, its entry routes and resulting consequences are not well understood. Here, we show a pronounced upregulation of interferon signaling pathways of the neurovascular unit in fatal COVID-19. By investigating the susceptibility of human induced pluripotent stem cell (hiPSC)-derived brain capillary endothelial-like cells (BCECs) to SARS-CoV-2 infection, we found that BCECs were infected and recapitulated transcriptional changes detected *in vivo*. While BCECs were not compromised in their paracellular tightness, we found SARS-CoV-2 in the basolateral compartment in transwell assays after apical infection, suggesting active replication and transcellular transport of virus across the blood-brain barrier (BBB) *in vitro*. Moreover, entry of SARS-CoV-2 into BCECs could be reduced by anti-spike-, anti-angiotensin-converting enzyme 2 (ACE2)-, and anti-neuropilin-1 (NRP1)-specific antibodies or the transmembrane protease serine subtype 2 (TMPRSS2) inhibitor nafamostat. Together, our data provide strong support for SARS-CoV-2 brain entry across the BBB resulting in increased interferon signaling.

INTRODUCTION

Severe acute respiratory syndrome coronavirus 2 (SARS-CoV-2) had infected over 280 million people and contributed to over 5.4 million deaths worldwide by December 28, 2021 (World Health Organization, https://covid19.who.int/). Although the disease primarily affects the respiratory system, damage and dysfunction have also been found in other organs, including the kidney, heart, liver, and brain (Puelles et al., 2020). Neurological and neuropsychiatric complications, such as cerebrovascular injury, encephalitis, encephalopathy, dizziness, headache, hypogeusia, and hyposmia, but also psychosis, neurocognitive syndrome, and affective disorders, have been reported in a significant number of patients (Mao et al., 2020; Woo et al., 2020). SARS-CoV-2 RNA and proteins have been detected in the brain and cerebrospinal fluid (CSF) of COVID-19 patients, but viral loads are comparatively low

and findings remain controversial (Matschke et al., 2020; Meinhardt et al., 2021; Puelles et al., 2020; Song et al., 2021). Despite numerous reports of neurological symptoms in COVID-19, it remains unclear whether these are a consequence of direct neural infection, parainfectious or post-infection immune-mediated disease, or sequelae of systemic disease (Ellul et al., 2020; Iadecola et al., 2020; Mao et al., 2020). Studies on brain tissue from deceased COVID-19 patients cannot address disease kinetics and underlying mechanisms, thus emphasizing the need for accessible and tractable experimental models to investigate SARS-CoV-2 cellular tropism, its functional impact, and therapeutic strategies.

Classic animal models are limited in their ability to recapitulate human COVID-19 symptoms and require non-physiological transgene-mediated overexpression of the human SARS-CoV-2 receptor angiotensin-converting enzyme 2 (ACE2) (Bao et al., 2020; Sun et al., 2020) or mouse-adapted virus strains to exhibit symptoms (Dinnon et al., 2020). Although cell lines have been used to study SARS-CoV-2 infection and test drug efficacy (Ellinger et al., 2021), they do not recapitulate human cell physiology and may lack key proteins required for viral entry, such as ACE2, transmembrane protease serine subtype 2 (TMPRSS2) (Hoffmann et al., 2020), or neuropilin-1 (NRP1) (Cantuti-Castelvetri et al., 2020; Daly et al., 2020). These limitations call for the development of human cellular models of SARS-CoV-2 infection that more faithfully recapitulate the function of individual tissues.

Human induced pluripotent stem cell (hiPSC)-based models provide a versatile platform to investigate the susceptibility of various cell types to viral infection and the resulting consequences. hiPSC-derived blood-brain barrier models were instrumental in studying infection with bacteria, viruses (including Zika virus), and fungal toxins (Alimonti et al., 2018; Kim et al., 2017; Kim and Schubert-Unkmeir, 2019; Martins Gomes et al., 2019; Patel et al., 2018). hiPSC-derived organoids have been used to model SARS-CoV-2 infection in many organs, including the vasculature (Monteil et al., 2020) and brain (Ramani et al., 2020). These experiments have shown that SARS-CoV-2 may infect and replicate within cells of multiple organs, leading to expression changes in genes linked to inflammatory responses and altered cellular functions.

Applying spatial transcriptomics, we show that transcriptional changes, in particular upregulation of interferon signaling pathways, are abundant in the neurovascular unit in COVID-19 patients. The neurovascular unit maintains the physiological function of the blood-brain barrier (BBB) and comprises brain capillary endothelial cells (BCECs) and includes other cell types, such as pericytes, astrocytes, neurons, and microglia (Hawkins and Davis, 2005). Key BBB functions are the maintenance of CNS homeostasis and the prevention of penetration of neurotoxic substances as well as pathogens, such as bacteria and viruses. To investigate the susceptibility of the BBB and specifically model SARS-CoV-2 infection in the endothelial cell layer of the neurovascular unit, we used hiPSC-derived brain capillary endothelial-like cells (hiPS-BCECs) in a transwell setup to mimic the interface between the two compartments: vessel (apical) and brain parenchyma (basolateral). After apical SARS-CoV-2 application, we observed entry into hiPS-BCECs, active replication, transcellular transport, and release of the virus at the basolateral side. Moreover, we present functional consequences at the cellular and molecular levels. Elucidating such mechanisms and assessing therapeutics in a readily accessible compartment might ameliorate disease severity and COVID-19-related CNS phenotypes.

RESULTS

The vascular niche is dysregulated in patients' brains in fatal COVID-19

Histopathological studies have demonstrated the presence of SARS-CoV-2 in different cell types of the brain parenchyma (Matschke et al., 2020; Meinhardt et al., 2021; Song et al., 2021). Entry routes into the brain may include the olfactory mucosa (de Melo et al., 2021; Meinhardt et al., 2021), the vasculature (Meinhardt et al., 2021), the brain stem or vagal nerve (Matschke et al., 2020), or neuronal transport (Song et al., 2021), but molecular mechanisms underlying neuroinvasion of SARS-CoV-2 remain ill defined. To identify specific molecular alterations in the neurovascular unit in COVID-19, we performed spatial transcriptomics of selected neurovascular units of cortex gray matter tissue in COVID-19 patients and controls (Table S1) by using the Nanostring Digital Spacial Profiler (DSP) platform (Figure 1A). Here, specific regions of interest (ROIs) in a tissue section can be selected by cell-type-specific immunofluorescence staining (Figure 1A). A set of labeled probes is hybridized to the RNA on the entire tissue section. Hybridized probes are collected by UV-light cleavage specifically at the chosen ROI and then further analyzed by Illumina sequencing to determine differential expression of respective genes, enabling spatial transcriptomic analysis of human *post mortem* brain tissue (Figure 1A). In our approach, we specifically selected ROIs surrounding cortical vessels for sequencing (Figure 1B). This allowed us to specifically characterize SARS-CoV-2-induced transcriptional changes at the neurovascular unit. By immunofluorescent staining of the astrocyte-specific marker glial fibrillary acidic protein (GFAP), the endothelial marker CD31, and the leukocyte marker CD45, we chose brain regions with comparable glial activation and

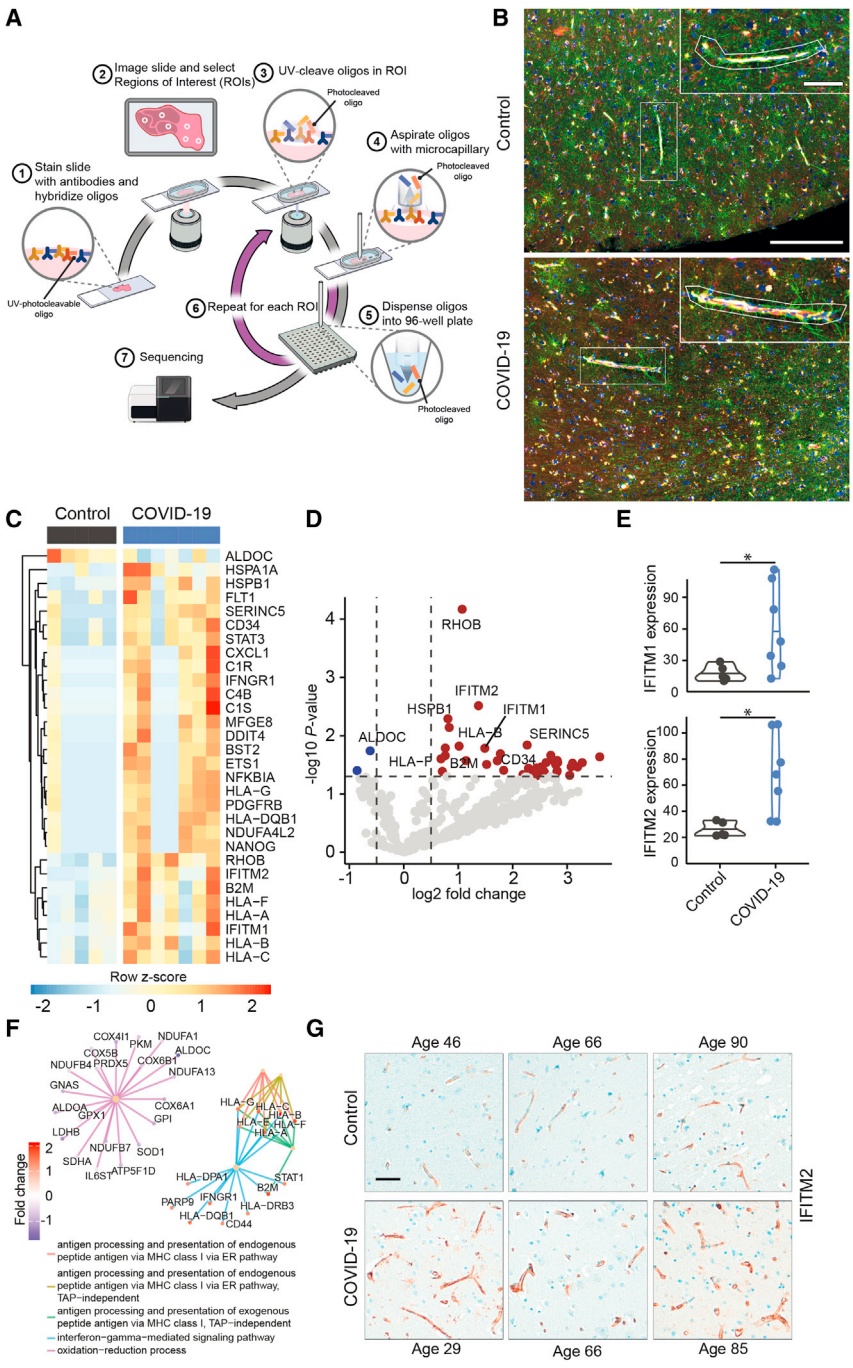

Figure 1. Transcriptional profiling of the neurovascular unit of COVID-19 and control brains

(A) Schematic representation of the spatial transcriptomic analysis of the neurovascular unit in human brain tissue with the Nanostring DSP platform. Brain tissue sections were stained for abundant cell populations (here: CD31, CD45, GFAP, and nuclei) and hybridized with a library of photocleavable probes for a specific gene panel. Regions of interest are chosen and illuminated, and the hybridized probes are collected only there. Downstream analyses of the collected probes provide a representative picture of RNA expression of genes of interest in this specific location, here, the neurovascular unit.

(B) Representative images of cortical regions of control (top) and COVID-19 brains (bottom), stained for GFAP (green), CD31 (yellow), CD45 (red), and DNA (blue). Two representative ROIs that were used for transcriptional analyses are shown. Scale bar, 250 μm; close up, 75 μm.

(C) Heatmap summarizing all differentially regulated genes. Gene-dependent h-clustering was performed. Color shows row *Z* score.

(D) Volcano plot showing differentially up- (red) and downregulated (blue) genes. Top differentially regulated genes are labeled.

(E) Normalized expression of *IFITM1* (top) and *IFITM2* (bottom). Shapiro-Wilk tests followed by Mann-Whitney U tests were performed. *p = 0.03 for *IFITM1*, *p = 0.01 for *IFITM2*.

(F) Gene set enrichment analysis of all detected genes. Color shows log2 fold change.

(G) Representative images for IFITM2 staining in brain tissue of control and COVID-19 patients. Images of age-matched pairs are displayed, demonstrating expression of IFITM2 in the neurovascular unit and its upregulation in fatal COVID-19. Scale bar, 50 μm.

immune cell infiltration of control and COVID-19 patients (Figure 1B). We selected ROIs in five control and seven COVID-19 specimens, with three to five vessels per individual cortex tissue, in total 48 vessels. ROIs contained an average of 27 cells as measured by nucleus count (ranging from n = 8 to n = 67) surrounding CD31$^+$ vessels, including mainly endothelial cells but also astrocyte endfeet and other cells (close up in Figure 1B). By using a conservative normalization and filtering approach and applying stringent cutoff criteria, we identified 30 differentially regulated genes (Figures 1C and 1D) in brain vessels of COVID-19 patients compared with controls. Of note, *IFITM1* and *IFITM2*, which are necessary for SARS-CoV-2 infection in human lung cells (Shi et al., 2021), were significantly upregulated (*p = 0.03 for *IFITM1*, *p = 0.01 for *IFITM2*) in COVID-19 patients (Figures 1D and 1E). Subsequent gene

set enrichment analysis (GSEA) revealed an upregulation of mRNAs related to antigen processing and major histocompatibility complex (MHC) class I-dependent antigen presentation (Figure 1F), supporting the notion that SARS-CoV-2 directly affects brain endothelial cells. In addition, we found that interferon-γ signaling was enhanced in COVID-19 (Figure 1F). To validate our findings, we performed immunohistochemical staining of IFITM2 in COVID-19 and control brains. Here, we could show that IFITM2 expression is restricted to the neurovascular unit and upregulated in COVID-19 patients (Figure 1G). In contrast to these highly specific transcriptional changes, the brain endothelial marker CD31 revealed no significant differences between COVID-19 and control brains (Figures S1A and S1B). Assessment of the abundance of the SARS-CoV-2 entry factors ACE2 and NRP1 in human cortex brain vessels revealed that NRP1 was more abundant than ACE2 (Figure S1C).

SARS-CoV-2 infects hiPS-BCECs

Since we detected a specific interferon signature in the neurovascular unit in COVID-19 patients, we wondered whether this could be due to direct infection and contact with SARS-CoV-2 or a more general immune phenotype. Thus, to determine whether the brain vasculature could be a potential entry point for SARS-CoV-2 into the brain, we aimed to investigate the susceptibility of human BCECs to SARS-CoV-2 infection. hiPSCs provide an effective cell source to generate functional BCECs, thereby enabling mechanistic studies. We applied existing protocols to generate hiPS-BCECs in transwell monolayer cultures (Appelt-Menzel et al., 2017; Lippmann et al., 2012, 2014) and could confirm expected morphology (Figure S2A), transcriptional profiles (Figure S2B), BCEC-specific marker expression (Figure S2C), an intact tight-junction (TJ) network (Figure S2D), transendothelial electrical resistance (TEER) values >1,000 $\Omega \cdot cm^2$ (Figure S2E), and permeability coefficients for paracellular tracer molecules like fluorescein (Figure S2F). Of note, we performed correlation analyses of transcripts derived from freshly prepared brain vessels of human brain biopsies and hiPS-BCECs and found a strong and significant correlation between the 100 highest and the 100 lowest expressing genes (Figures S3A and S3B).

We infected hiPS-BCECs from the apical side of the transwell model, mimicking an infection from the endovascular compartment. One day post-infection, we detected SARS-CoV-2 N and spike proteins in infected hiPS-BCECs (Figure 2A). Infection with different MOIs (MOI 0.1, 1, and 10) using two independent SARS-CoV-2 isolates (Pfefferle et al., 2020a; Zimniak et al., 2021) resulted in a dose-dependent increase in the number of infected cells (Figure 2B). Of note, a human brain endothelial cell line, hCMEC/D3, could not be infected with SARS-CoV-2 (Figure S4), explicable by the ectopic ACE2 expression required to infect that model (Wenzel et al., 2021). In hiPS-BCECs, we could stain for double-stranded RNA (dsRNA) in a subset of N-protein-positive infected cells, indicating active virus replication (Figure 2C). Already after 16 h post-infection we detected a significant increase (*p = 0.027) of SARS-CoV-2 RNA by qRT-PCR in the basolateral compartment compared with a transwell setting without the BCEC layer (Figure 2D), without compromising the integrity of the BBB with regard to paracellular permeability to fluorescein (Figure 2E). We therefore speculate that the basolateral abundance of viral particles could be a consequence of active virus production, transcellular transport, and release from the hiPS-BCECs. The SARS-CoV-2 entry receptor ACE2 and co-factor/alternative receptor TMPRSS2 and NRP1 are all expressed in hiPS-BCECs as detected by qRT-PCR, with *NRP1* being the most abundant (Figure 2F), similar to the situation in human brain tissue (Figure S1C). A non-significant decrease of mRNA expression was observed for all three genes after SARS-CoV-2 exposure, a hallmark of infection (Glowacka et al., 2010). Importantly, the increase of *IFITM1* and *IFITM2* expression observed in tissue infected with SARS-CoV-2 could be recapitulated in our model by both mRNA sequencing (*p = 0.031 for *IFITM1*, p = 0.403 for *IFITM2*) and qRT-PCR (Figure 2G). In transmission electron microscopy (TEM) cross sections of SARS-CoV-2-treated hiPS-BCECs, we could confirm attachment and apical uptake as well as basolateral shedding of the virus (Figures 2H–2J). After infection, neighboring hiPS-BCECs remained connected by complex TJs constricting the paracellular space (Figure 2K). Furthermore, adhesion points anchored within the actin filament network were detected, indicating the integrity of cell-cell contacts (Figure 2K). As reference, TEM images of uninfected hiPS-BCECs are shown in Figure S2D. The overall integrity of the hiPS-BCECs was further demonstrated by intact localization and unaltered expression of TJP1/ZO-1, a TJ marker, after infection (Figure 2L).

Virus-related transcriptional dysregulation in hiPS-BCECs mirrors *in vivo* findings

To compare the transcriptional response of the neurovascular unit in COVID-19 patients with that of SARS-CoV-2-infected hiPS-BCECs, we mock infected hiPS-BCECs or applied SARS-CoV-2 virus for 24 h and performed mRNA sequencing (Figures 3A and S3C). In line with our findings from spatial transcriptomics of brain vessels and their microenvironment in fatal COVID-19 (Figure 1), we detected that genes responsible for the innate immune response and type I interferon response were significantly upregulated. Moreover, genes that regulate phosphorus-dependent metabolic and ATP-generating pathways were

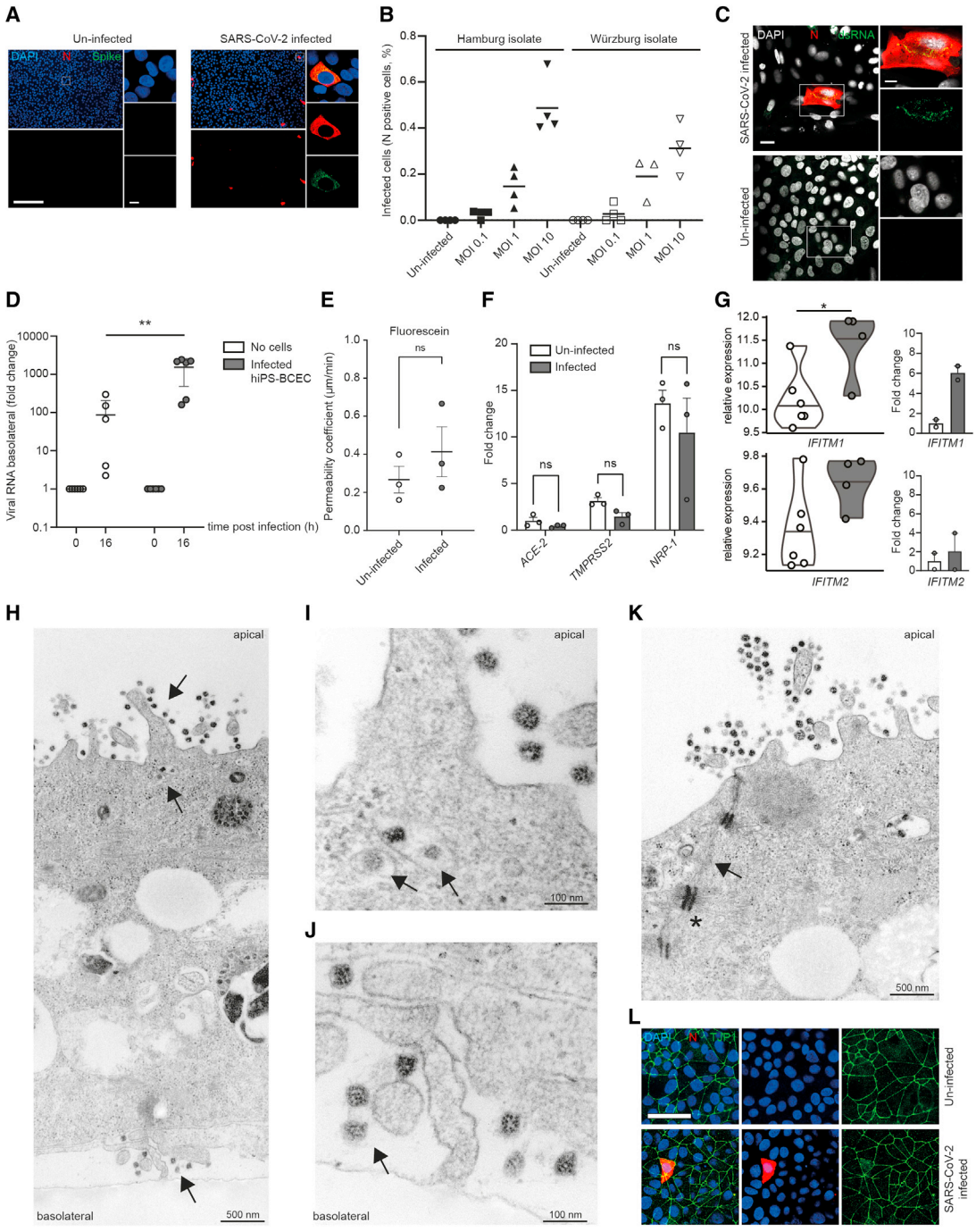

Figure 2. SARS-CoV-2 infects and replicates in hiPS-BCECs

(A) Representative overview images that were used for subsequent quantification and respective close ups of N and spike protein double staining after infection with SARS-CoV-2 for 24 h (MOI 10) are shown. In the overview images, N protein is oversaturated to enable easy counting of infected cells; the close ups display the subcellular localization of N and spike protein in infected cells. Uninfected cells served as control and did not show any staining with SARS-CoV-2-specific antibodies. SARS-CoV-2 N protein (red), SARS-CoV-2 spike protein (green), counterstained by DAPI (blue). Scale bar, 200 µm; close up, 7.5 µm.

(B) Infected hiPS-BCECs (MOI 0.1, 1, and 10 each for Hamburg and Würzburg isolates) stained for N protein, indicating a dose-dependent rate of infection; n = 2 independent experiments, three or four technical replicates per condition.

(legend continued on next page)

significantly downregulated (Figures 3B–3D), which is in accord with studies in SARS-CoV-2-infected lung organoids (Pei et al., 2020). To analyze the translatability to humans and further support the validity of our model, we compared the biological themes of SARS-CoV-2-infected hiPS-BCECs with our spatial transcriptomics data from COVID-19 brain vasculature. Intriguingly, SARS-CoV-2 infection of endothelial cells consistently resulted in downregulation of metabolic pathways and upregulation of a cellular interferon response (Figure 3E). Of note, upregulated biological themes in COVID-19 brain vasculatures were significantly enriched (normalized enrichment score [NES] = 2.3, **p = 0.007), whereas downregulated biological themes were significantly de-enriched (NES = −1.7, *p = 0.01), in our SARS-CoV-2-infected hiPS-BCECs (Figure 3F). We thus show that brain endothelial cells show intrinsic inflammatory profiles upon contact with SARS-CoV-2, independent of immune cells. In summary, this highlights the usefulness of our *in vitro* model to study the BBB alterations in COVID-19, which is key to prospective mechanistic and pharmacological studies.

SARS-CoV-2 infection of hiPS-BCECs can be pharmacologically inhibited

To investigate whether our hiPS-BCEC transwell system provides a suitable model to probe therapeutic intervention strategies, we went on to investigate the ability of blocking antibodies to prevent hiPS-BCEC infection by SARS-CoV-2. We infected the hiPS-BCEC transwell model from the apical (lumen-facing) side in either the presence or the absence of anti-spike antibodies targeting the receptor-binding domain (RBD) required for viral entry into the cell. After 24 h, SARS-CoV-2 RNA was quantified in the apical and basolateral compartments by qRT-PCR. SARS-CoV-2 RNA was significantly increased (*p = 0.0132) in the basolateral compartment in untreated cells, an effect that could be mitigated by anti-spike-specific antibodies (Figure 4A). In addition, we tested reagents targeting viral uptake, including anti-spike, anti-ACE2, and anti-NRP1 antibodies and the protease inhibitor nafamostat, which inhibits TMPRSS2 with nanomolar potency in cell-based assays (Ellinger et al., 2021). Here, we infected the apical side with SARS-CoV-2 in the absence or presence of respective inhibitory molecules. Immunofluorescence staining of N-protein-positive cells compared with all cells was used to quantify SARS-CoV-2 infection (Figure 4B). Of note, all antibodies and nafamostat could significantly (****p < 0.0001) diminish virus uptake by hiPS-BCECs (Figure 4C).

DISCUSSION

A substantial number of COVID-19 patients exhibit neurological symptoms, which may be further influenced by different host factors such as age, sex, comorbidities, disease progression, and others (Helms et al., 2020; Puelles et al., 2020; Solomon et al., 2020). The exact mechanism of how SARS-CoV-2 may enter the brain is currently unknown. The main hypotheses are neuron-to-neuron spread via bipolar cells located in the olfactory epithelium (de Melo et al., 2021; Meinhardt et al., 2021), a

(C) Representative immunofluorescence of SARS-CoV-2-infected hiPS-BCECs stained for N protein (red) and double-stranded RNA (dsRNA, green) (MOI 10), counterstained by DAPI (white). Uninfected hiPS-BCECs served as control. Scale bar, 25 μm; close up, 10 μm.
(D) In transwell assays, SARS-CoV-2 is applied from the apical side to infect hiPS-BCECs (MOI 10). Mean ± SEM of n = 3 independent experiments, three technical replicates per condition. A significant increase in viral RNA was detected in the basolateral compartment by qRT-PCR. Two-way ANOVA with *post hoc* Sidak's multiple comparison test, **p = 0.001.
(E) Fluorescein transport study. The permeability coefficient is comparable 24 h post-infection for SARS-CoV-2 (MOI 10) or control-treated samples. Mean ± SEM from n = 3 independent experiments. Unpaired Student's t test, p > 0.05.
(F) Host factors required for SARS-CoV-2 uptake are expressed in hiPS-BCECs and are diminished 24 h post-infection (MOI 10) compared with uninfected cells. Normalized to ACE2 in uninfected cells. Mean ± SEM from n = 3 individual experiments. Two-way ANOVA with *post hoc* Sidak's multiple comparison test, p > 0.05.
(G) Normalized expression of *IFITM1* and *IFITM2*. Left: differential expression analysis of RNA-sequencing data with false discovery rate (FDR) correction for multiple comparisons. *p = 0.031 for *IFITM1*, p = 0.403 for *IFITM2*. Violin plots and mean of n = 6 independent experiments (uninfected) and n = 4 independent experiments (infected) are shown. Right: differential expression analysis of qRT-PCR data. Mean ± SEM of n = 2 experiments with independent virus isolates, three technical replicates per condition.
(H–K) TEM micrographs of SARS-CoV-2-infected hiPS-BCECs. (H) Overview of a TEM cross section of a hiPS-BCEC monolayer. After infection (MOI 10) from the apical side (top black arrow), virus is taken up, is evident in intracellular vesicles (middle black arrow), and is released from the cells on the basolateral side (bottom black arrow). (I and J) Detailed areas in higher resolution from (H). (I) Virus is evident in intracellular vesicles (black arrows). (J) Virus is released from the cells on the basolateral side (black arrow). (K) Neighboring hiPS-BCEC monocultures are connected by complex TJs constricting the paracellular space (black arrows). Furthermore, adhesion points (*punctum adherens*, black asterisk in K) anchored within the actin filament network were detected, indicating the integrity of cell-cell contacts. Scale bars as indicated.
(L) Representative immunofluorescence of SARS-CoV-2-infected hiPS-BCECs stained for SARS-CoV-2 N (red) and TJP1 (green) proteins show intact cell connectivity 24 h post-infection (MOI 10), counterstained by DAPI (blue). Scale bar, 50 μm.

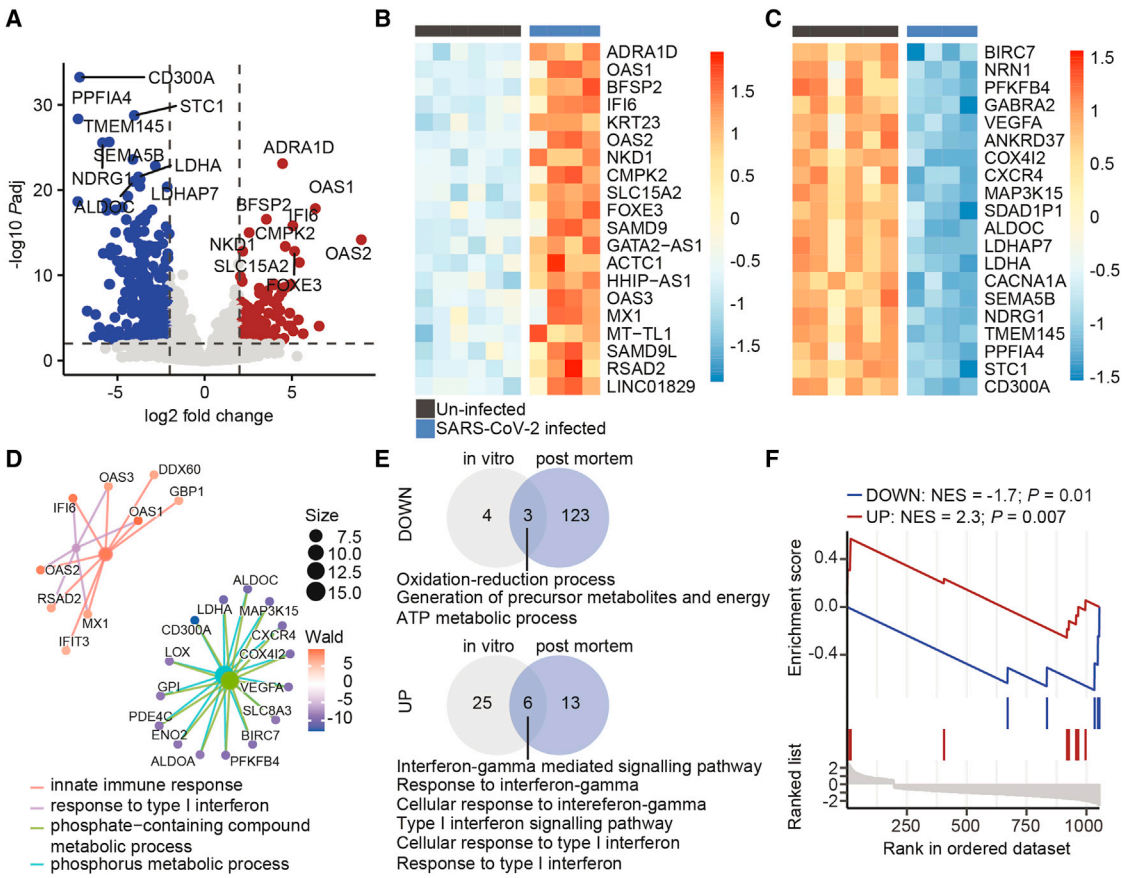

Figure 3. Transcriptional profiling of SARS-CoV-2-infected hiPS-BCECs

(A) Volcano plot depicting differentially up- (red) and downregulated (blue) genes. Horizontal line shows −log10 of 0.01; vertical lines show log2 fold change of −1 and 1.

(B) Heatmap depicting top 20 upregulated genes in SARS-CoV-2-infected hiPS-BCECs (MOI 10). Color shows row *Z* score.

(C) Heatmap depicting top 20 downregulated genes in SARS-CoV-2-infected hiPS-BCECs. Color shows row *Z* score.

(D) GSEA of top 200 upregulated and top 200 downregulated genes. Color shows results of Wald statistics; size shows number of identified genes for each gene ontology (GO) term.

(E) Overlap of downregulated (top) and upregulated (bottom) biological themes of SARS-CoV-2-infected hiPS-BCECs (MOI 10) and blood vessels from COVID-19 brains.

(F) Enrichment analysis of upregulated (NES = 2.3, **p = 0.007) and downregulated (NES = −1.7, *p = 0.01) biological themes of blood vessels from COVID-19 brains in SARS-CoV-2-infected blood hiPS-BCECs. NES, normalized enrichment score. Data from n = 3 independent differentiation experiments, one or two replicates each.

hematogenous route across the blood-CSF barrier (Desforges et al., 2014; Song et al., 2021), or transport via the vagal nerve to the brain stem (Matschke et al., 2020). Other routes of migration across the BBB, for example, transmigration of SARS-CoV-2-carrying leukocytes, cannot be excluded. Shortcomings of these studies relate to their non-mechanistic approaches or non-physiological animal models, which have been summarized recently (Butowt et al., 2021). In the work presented here, we systematically studied the brain vasculature as a potential entry site for SARS-CoV-2: initially, we performed spatial transcriptomics on *post mortem* COVID-19 and control brain tissue, focusing on the transcriptional changes in the neurovascular unit. We identified a significant upregulation of interferon-γ-mediated signaling pathways, including those coding for IFITM1 and IFITM2, which have been reported to potentially restrict SARS-CoV-2 infections (Shi et al., 2021). Second, we applied a transwell model of hiPS-BCECs that resembles human BCECs in their morphology, transcriptome, marker expression, and functional properties. In this model, we could observe entry and replication of SARS-CoV-2. Detailed analysis of these cells by electron microscopy showed virus uptake on the apical, lumen-facing side of

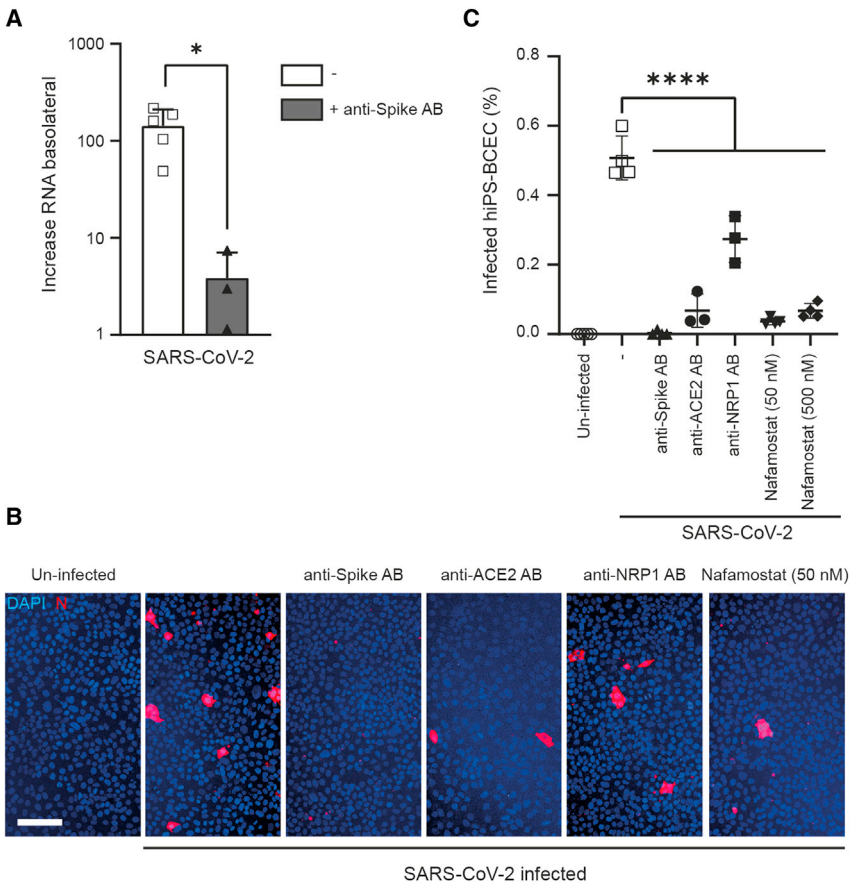

Figure 4. SARS-CoV-2 infection of hiPS-BCECs can be diminished by blocking antibodies and small-molecule protease inhibitors

(A) In transwell assays, SARS-CoV-2 was used to infect hiPS-BCECs from the apical side (MOI 10). An increase in viral RNA was detected in the basolateral compartment by qRT-PCR. This effect could be significantly diminished by administration of anti-spike antibodies. Mean ± SEM of n = 3 independent experiments, one or two technical replicates each. Unpaired Student's t test, *p = 0.0132.

(B) Image-based assessment of hiPS-BCECs after SARS-CoV-2 infection (MOI 10). Anti-spike, anti-ACE2, and anti-NRP1 antibodies and nafamostat (50 and 500 nM) were applied to counteract infection. Cell counting was performed using ImageJ software after staining SARS-CoV-2 N-protein-positive cells (red), counterstained by DAPI (blue). Scale bar, 100 μm.

(C) Quantification of (B). Mean ± SEM of n = 3 independent experiments, one or two technical replicates each. One-way ANOVA followed by Dunnett's multiple comparisons test, ****p < 0.0001.

the transwell model, active replication within the cells, transcellular transport, and shedding of viral particles on the basolateral, brain-mimicking side. This is in line with previous reports of BBB crossing of isolated spike protein in mice (Rhea et al., 2021) and in BBB *in vitro* models (Buzhdygan et al., 2020). Of note, the transcriptional changes observed in the neurovascular unit in COVID-19 patients, in particular an upregulation of interferon-γ-mediated signaling pathways and a downregulation of metabolic processes, could be recapitulated in this model. Thus, our study on one hand defines the molecular consequences of SARS-CoV-2 infection for the neurovascular unit but on the other hand also provides a means to investigate the cellular susceptibility, pathophysiology, and treatment strategies for SARS-CoV-2 infection of BCECs and subsequent brain infection and inflammation.

Building upon previous findings (Lippmann et al., 2012, 2014), we utilized an hiPS-BCEC model that is simple, robust, and reproducible with the initial goal to study the impact of SARS-CoV-2 infection and its molecular consequences on the BBB. The hiPS-BCECs exhibit a transcriptome that is highly comparable to that of freshly isolated brain vessels from human brain biopsies. Upon infection, the hiPS-BCEC model develops SARS-CoV-2-induced pathophysiological hallmarks at cellular and molecular levels, in particular a significant upregulation of genes involved in interferon signaling pathways. Of note, our findings indicate that endothelial cells might show an upregulation of interferon signaling after contact with SARS-CoV-2 that is independent of an immune cell contribution.

ACE2 has been identified as a key cell entry receptor for SARS-CoV-2 (Hoffmann et al., 2020). Low to moderate ACE2 expression has been detected in various brain regions, including the choroid plexus in humans and mice (Chen et al., 2020). Recent studies suggest that other proteins, such as NRP1, facilitate SARS-CoV-2 entry (Cantuti-Castelvetri et al., 2020; Daly et al., 2020). We here report expression of ACE2, confirming previous data (Matschke et al., 2020), but a higher relative abundance of *NRP1* mRNA and protein in BCECs and hiPS-BCECs. Furthermore, our pharmacological blocking experiments confirm that both TMPRSS2 and NRP1 are involved in the entry of SARS-CoV-2 and may serve as promising intervention targets. Interestingly, although ACE2 expression was

comparatively low in our BCEC model, incubation with an anti-ACE2 antibody almost completely blocked infection, highlighting the importance of ACE2 as a SARS-CoV-2 entry factor.

Limitations of the study

Our study demonstrates the susceptibility of hiPS-BCECs to SARS-CoV-2 infection *in vitro*. Moreover, we provide a thorough analysis of brain samples from individuals with COVID-19 suggesting that SARS-CoV-2 contact or viral entry via the BBB results in significant changes that might at least partially explain neurological symptoms in COVID-19. Direct evidence of SARS-CoV-2-infected brain endothelial cells *in vivo* by staining of viral antigens, however, is not presented here and is still under debate, although respective data have been published (Schwabenland et al., 2021). Our methodology has a number of constraints that may limit overall result interpretation. Direct exposure of hiPS-BCEC cultures to SARS-CoV-2 in the culture medium may not accurately recapitulate the physiological entry process in humans. Exposure of cells to large amounts of virus might possibly result in forced uptake with an entry via alternative routes. Our pharmacological experiments provide evidence of receptor-mediated entry in our model, since it could be efficiently and specifically blocked by specific antibodies despite high virus titers. Moreover, we showed that low MOI (as low as MOI 0.1) still leads to virus entry in hiPS-BCECs.

Also, given the comparatively low viral load (<1,000 SARS-CoV-2 RNA copies/mL) in the basolateral compartment, assessment of infectivity (e.g., via plaque assays) has not been possible in our model and experimental setting. For this, we would have to (1) significantly upscale our model or (2) incubate it for a much longer period of time, which is impossible due to a reported breakdown of barrier integrity at day 11 of the protocol (independent of virus) (Hollmann et al., 2017) and resulting leakage of virus to the basolateral compartment.

Regarding cellular identity, a recent study (Lu et al., 2021) challenges the hiPS-BCEC model applied here (Lippmann et al., 2012), which was further refined, evaluated, and widely applied over the last decade, including for the study of the biology of infection. Lu et al. claim that this differentiation protocol does not generate cells of endothelial but of epithelial origin. Opposed to the findings by Lu et al., we here report an increase in endothelial transcripts during the course of differentiation (e.g., *VWF*, *CDH5*, *ABCG2*, *ABCB1*) for two independent hiPSC lines (WISCi004-B and ZIPi013-B) and specific staining of key BCEC marker proteins (including CLDN5) after completion of the differentiation protocol, in line with other publications in the field (Appelt-Menzel et al., 2017; Lim et al., 2017; Lippmann et al., 2020). It is well appreciated that hiPSC-based models can show a lack of maturity in expression signatures and function. Therefore, epithelial expression signatures from pluripotent stem cells might be maintained after differentiation, as shown here for *CLDN3*, *CLDN6*, and *CLDN7*, which Lu et al. describe as epithelial markers. Having said this, several studies using human primary BCECs and hiPS-BCECs have been published over the past few years reporting the expression of almost all claudins in human BBB *in vitro* models (Delsing et al., 2018; Lim et al., 2017; Vatine et al., 2017). Of note, the alternative protocol suggested by Lu et al. cannot achieve a high paracellular tightness comparable to that of the physiological situation *in vivo*, which is of importance for our SARS-CoV-2 model to reliably test the molecular and functional consequences of infection and pharmacological treatment strategies. All our data were generated with hiPS-BCEC transwell inserts of TEER values >1,000 $\Omega \cdot cm^2$ on day 10 of differentiation; inserts with lower values were not used for subsequent analysis.

Interestingly, the established hCMEC/D3 model could not be infected in our hands, pointing toward the suitability of the hiPS-BCEC model to study SARS-CoV-2-related phenomena.

The hiPS-BCEC transwell model applied here lacks additional cell types of the neurovascular unit, such as pericytes, astrocytes, and microglia, which may contribute to disease pathogenesis *in vivo*. Moreover, the model lacks immune cells, such as T cells and monocytes, which have been shown to mediate host responses to SARS-CoV-2 infection, including tissue-specific inflammation (Tay et al., 2020). Of note, our BCEC model displayed an intrinsic inflammatory profile after contact with SARS-CoV-2. Since endothelial cells are major targets of SARS-CoV-2, they may be the primary cause of SARS-CoV-2-related effects in the brain, with neurological symptoms being secondary to vascular changes and hypoxia (Ellul et al., 2020).

We here report that interferon signaling was increased in brain vessels in fatal COVID-19 when assessed by Nanostring DSP analysis. To enable expression analyses in *post mortem* tissue, we specifically sampled COVID-19 brain tissue with short *post mortem* and formalin fixation time. However, control tissue of the same quality was not available for Nanostring DSP analysis in required quantities; thus, we also included brain biopsies with short fixation times. Those tissues might not be an optimal control; however, over-fixed control tissues would likewise have been suboptimal. To overcome these limitations, we performed IFITM2 staining in our full panel of COVID-19 and control tissues, including biopsies and autopsies. With this approach, we could show that changes in IFITM2 are restricted to the neurovascular unit and specifically upregulated in COVID-19.

It is currently unclear whether neurological symptoms in COVID-19 are a direct result of neural infection or secondary to endothelial cell infection, hypoxia, or circulating pro-inflammatory cytokines. Future studies of SARS-CoV-2 susceptibility can extend to a more complex *in vitro* model of the neurovascular unit. Our *in vitro* studies provide useful information about specific cell types of focus for future human studies and offer a simple, accessible, and tractable human cell platform to investigate cellular susceptibility, disease mechanisms, and treatment strategies for SARS-CoV-2 infection of the human brain.

EXPERIMENTAL PROCEDURES

Human samples

Autopsies were performed at the Institute of Legal Medicine of the University Medical Center, Hamburg-Eppendorf, Germany. Use of *post mortem* human tissue and use of surgically removed brain specimens after conclusion of diagnostic procedures were reviewed and approved by the institutional review board of the independent ethics committee of the Hamburg Chamber of Physicians (protocol nos. PV7311, 2020-10353-BO-ff, and PV5034). Frontal/temporal cortex brain tissues were used for this study. For COVID-19, *post mortem* tissue samples were used; for non-COVID-19 controls, we added biopsy samples from patients undergoing neurosurgery for epilepsy. qPCR analysis of SARS-CoV-2 expression was already published elsewhere (Matschke et al., 2020) but is included in Table S1 (epidemiological and clinical information of COVID-19 patients and controls). For Nanostring DSP expression analysis, only samples with short formalin fixation times (24–96 h) were selected, to ensure high RNA quality. Cortical regions selected for Nanostring DSP were free of apparent inflammatory changes and displayed normal and non-activated morphology.

The use of human cells for the generation of hiPSCs was approved by the ethics committee of the Universitätsklinikum Schleswig-Holstein, Campus Kiel, Germany (A145/11) and is further described at https://www.sciencellonline.com/technical-support/ethical-statement.html.

Nanostring digital spatial profiling

Individuals selected for Nanostring DSP are labeled by # in Table S1. Mean age for Nanostring DSP expression analysis was 72 years for COVID-19 patients (29–89 years) and 57 years for controls (46–66 years). Regions of gray matter were selected from existing paraffin blocks of formalin-fixed cortex brain tissues from COVID-19 patients or controls; 5 mm tissue punches were prepared, and two new paraffin blocks were poured, each containing six different tissue punches. Tissue sections (5 μm) were mounted on slides, deparaffinized, and processed according to published protocols (Merritt et al., 2020). RNA-preserving antigen retrieval was performed, followed by RNA target exposure with proteinase K. *In situ* hybridization of the probe panel (GeoMx Cancer Transcriptome Atlas [CTA] panel [1,825 targets] + COVID-19 targets spike-in) on the tissue sections was performed overnight at 37°C, followed by stringent washes to remove off-target probes. Subsequently, the morphology markers CD31 (vessel endothelium, 1:50; #ab212712, Abcam), GFAP (astrocytes, 1:400; #53-9892-82, Invitrogen), CD45 (leukocytes, 1:100; #13917BF, CST), and DNA (SYTO83, 1:25; Thermo Fisher Scientific) were used to visualize target regions. Three to five vessels per individual cortex tissue were selected with the custom polygon ROI tool. These selected areas were illuminated individually via UV light on a GeoMx digital spatial profiler, resulting in photocleavage of oligonucleotides present within each ROI. The oligonucleotides were collected in a 96-well microwell plate. Each GeoMx DSP aspirate in the plate contained photocleaved DNA oligos comprising an analyte identifier, a unique molecular identifier (UMI) barcode, and a primer binding site. When PCR was performed on the aspirates, Illumina adapter sequences and unique dual-sample indices were added. The final library was used for sequencing on an Illumina NGS platform using a dual-index workflow after a pooling and quality control process. Signal-based normalization was performed by normalizing the signal of each probe against the 75th percentile of the cumulative signal of the respective ROI. For subsequent analysis, we calculated the average normalized expression value for each gene of all ROIs of each individual. We compared control and COVID-19 by a mixed linear model using the *limma* package within the R environment (Ritchie et al., 2015). GSEA (Merico et al., 2010) was performed using the *clusterprofiler* package (Yu et al., 2012).

SARS-CoV-2 molecular diagnostics and qRT-PCR of host gene expression

Detection and quantification of SARS-CoV-2 RNA were performed as described previously (Norz et al., 2020; Pfefferle et al., 2020b). For verification of mRNA expression of the SARS-CoV-2 receptor genes, cellular RNA was extracted using TRIzol reagent (Thermo Fisher Scientific) as recommended by the manufacturer. Commercially available TaqMan assays were performed (*ACE2* [assay Hs01085333_m1], *TMPRSS2* [assay Hs01122322_m1], *NRP1* [assay Hs00826128_m1], *IFITM1* [Hs01652522_g1], *IFITM2* [Hs04194297_g1], all Thermo Fisher Scientific) using the RNA process control kit (Roche) on a Light Cycler 480 II instrument (Roche). We calculated gene expression as $2^{-\Delta Ct}$ relative to *GAPDH* (human, assay Hs02786624_g1, Thermo Fisher Scientific) as the endogenous control.

Vero cell culture and SARS-CoV-2 isolates

Vero cells (ATCC CRL-1006) were cultivated and maintained under standard conditions (Pfefferle et al., 2020a). The MOI was determined by plaque assays. In all infection experiments, SARS-CoV-2 isolate HH-1 (Pfefferle et al., 2020a) was used at an MOI of 10 unless stated otherwise. In addition, SARS-CoV-2 isolate Würzburg (Zimniak et al., 2021) was used for experiments in Figure 2B. Furthermore, the MOIs for individual experiments are indicated in the respective figure legends.

hiPS-BCEC differentiation and establishment of the *in vitro* BBB model

The differentiation protocol was adapted from previously published protocols (Appelt-Menzel et al., 2017; Lippmann et al., 2012, 2014). A graphical overview of the procedure is provided in Figure S2A. See supplemental information for details.

SARS-CoV-2 infection of hiPS-BCEC and pharmacological treatment

hiPS-BCECs were cultivated as described above. At day 10 of differentiation, cells were prepared for SARS-CoV-2 infection. For this, virus was mixed in EC medium with the respective antibody or small-molecule inhibitor. Anti-spike antibody (NI-607.531_C8, Neurimmune) was used at 1 nM, anti-ACE2 antibody at 2 μg/mL (AF933; R&D Systems [Hoffmann et al., 2020]), and anti-NRP1 at 2.5 μg/mL (MSB178289, MyBioSource) combined with anti-NRP1 at 10 μg/mL (HPAB-0514-CN; Creative Biolabs) or the serine protease (TMPRSS2) inhibitor nafamostat at 50 or 500 nM. The mixtures were added to the apical transwell compartment. Experiments were stopped after 24 h by fixation of cells with 4% formalin, and medium was harvested for qRT-PCR. The number of infected cells was quantified by fluorescence staining of SARS-CoV-2 N protein and ImageJ.

mRNA sequencing

RNA sequencing libraries were prepared using the TruSeq stranded mRNA Library Prep Kit (Illumina) according to the manufacturer's manual (document 1000000040498 v00) with a minimum total RNA input of 150 ng per sample. Libraries were pooled and sequenced on a NovaSeq 6000 sequencer (Illumina) generating 50 bp paired-end reads. The reads were aligned to the Ensembl human reference genome (GRCh38) using STAR v.2.4 (Dobin et al., 2013) with default parameters. The overlap with annotated gene loci was counted with featureCounts v.1.5.1 (Liao et al., 2014). Differential expression analysis was performed with DESeq2 (v.3.12) (Love et al., 2014) calling genes with a minimal 2-fold change and false discovery rate (FDR)-adjusted $p < 0.05$ differentially expressed. Gene lists were annotated using biomaRt (v.4.0) (Durinck et al., 2009). GSEA was performed using the *clusterprofiler* package (Yu et al., 2012).

Statistical analysis

The statistical analyses were carried out using GraphPad Prism (v.9.0.2, Windows 10 Enterprise). Images were analyzed using the PerkinElmer Columbus Image Data Storage and Analysis System (PerkinElmer) or ImageJ (NIH). Transcriptional data were analyzed within the R environment (v.1.2.5001) on a Mac OS X. All data were checked for normality before further analysis and means ± SEM were plotted. Depending on the data analyzed, differences between experimental groups were determined as indicated in the respective sections. Significant results are indicated by $*p < 0.05$, $**p < 0.01$, $***p < 0.001$, and $****p < 0.0001$.

Data and code availability

The code generated to analyze spatial transcriptomics is available from the corresponding author upon request. The accession number for the mRNA-sequencing data reported in this paper is GEO: GSE179923 (https://www.ncbi.nlm.nih.gov/geo/query/acc.cgi?acc=GSE179923).

SUPPLEMENTAL INFORMATION

Supplemental information can be found online at https://doi.org/10.1016/j.stemcr.2021.12.011.

AUTHOR CONTRIBUTIONS

S.K. conducted most staining experiments and related analysis of brain and hiPSC-derived tissues with support from E.T.; S.K., J.M., and M.G. performed neuropathological analysis; U.H., A.A.M., A.C., J.B., J.L., A.G., A.B., and W.N. established and characterized the hiPS-BCEC transwell model; S.P., N.G., E.-M.K., and J.B. performed all SARS-CoV-2 infections and related experiments; M.S.W. analyzed and visualized transcriptomic data; M.S. performed TEM experiments and analyzed the data; K.H., J.L.L., and D.S.F. assisted with the histological assessment of brain vessels; F.H., J.M., F.R., T.S., J.S., A.F., and B.O. autopsied the cases and provided autopsy or biopsy samples from COVID-19 patients and controls; S.F. and A.F. performed mRNA-sequencing experiments; S.M. provided anti-spike antibodies; F.J.M. assisted with the PluriTest analysis; S.K., A.A.M., J.B., G.G., C.C., A.K., P.G., B.O., M.A.F., M.G., and O.P. provided funding for the study; U.H., S.M., A.K., A.Z., and P.G. assisted with pharmacological experiments with antibodies and small molecules; S.K., U.H., S.P., M.S.W., M.A.F., M.G., and O.P. designed experiments for the study and analyzed the data; O.P. wrote the initial version of the manuscript; S.K., U.H., S.P., M.S.W., M.A.F., and M.G. revised the manuscript; S.K. and O.P. conceived and supervised the study. All co-authors contributed to the editing and discussion of the manuscript and approved the final version.

CONFLICT OF INTERESTS

The authors declare no competing interests.

ACKNOWLEDGMENTS

This work was supported by the German Federal Ministry of Education and Research (Bundesministerium für Bildung und Forschung, BMBF) for the projects HiPSTAR (01EK1608A to A.A.M. and 01EK1608B to O.P.) and DEFEAT PANDEMICs (01KX2021), by the internal "Anti-Corona" programs of the Fraunhofer-Gesellschaft (DRECOR, 840260, and iCARE, 602015), by the Deutsche Forschungsgemeinschaft (FR1720/18-1 to M.A.F. and GL589/10-1 to M.G.), and by the Hamburg Ministry of Labour, Health, Family Affairs and Integration. The Nanostring DSP work was supported by a COVID-19 grant from Nanostring to S.K. We thank the UMIF of the UKE for access to the microscope facility. We thank Emanuela Szpotowicz (Morphology and Electron Microscopy Core Facility) for excellent technical assistance. We thank Philine Lange (Institute of Legal Medicine) for helpful assistance. Our condolences to the families and all those who have lost their loved ones during the pandemic.

Received: July 12, 2021
Revised: December 15, 2021
Accepted: December 16, 2021
Published: January 20, 2022

REFERENCES

Alimonti, J.B., Ribecco-Lutkiewicz, M., Sodja, C., Jezierski, A., Stanimirovic, D.B., Liu, Q., Haqqani, A.S., Conlan, W., and Bani-

Yaghoub, M. (2018). Zika virus crosses an in vitro human blood brain barrier model. Fluids Barriers CNS *15*, 15.

Appelt-Menzel, A., Cubukova, A., Gunther, K., Edenhofer, F., Piontek, J., Krause, G., Stuber, T., Walles, H., Neuhaus, W., and Metzger, M. (2017). Establishment of a human blood-brain barrier co-culture model mimicking the neurovascular unit using induced pluri- and multipotent stem cells. Stem Cell Rep. *8*, 894–906.

Bao, L., Deng, W., Huang, B., Gao, H., Liu, J., Ren, L., Wei, Q., Yu, P., Xu, Y., Qi, F., et al. (2020). The pathogenicity of SARS-CoV-2 in hACE2 transgenic mice. Nature *583*, 830–833.

Butowt, R., Meunier, N., Bryche, B., and von Bartheld, C.S. (2021). The olfactory nerve is not a likely route to brain infection in COVID-19: a critical review of data from humans and animal models. Acta Neuropathol. *141*, 809–822.

Buzhdygan, T.P., DeOre, B.J., Baldwin-Leclair, A., Bullock, T.A., McGary, H.M., Khan, J.A., Razmpour, R., Hale, J.F., Galie, P.A., Potula, R., et al. (2020). The SARS-CoV-2 spike protein alters barrier function in 2D static and 3D microfluidic in-vitro models of the human blood-brain barrier. Neurobiol. Dis. *146*, 105131.

Cantuti-Castelvetri, L., Ojha, R., Pedro, L.D., Djannatian, M., Franz, J., Kuivanen, S., van der Meer, F., Kallio, K., Kaya, T., Anastasina, M., et al. (2020). Neuropilin-1 facilitates SARS-CoV-2 cell entry and infectivity. Science *370*, 856–860.

Chen, M., Shen, W., Rowan, N.R., Kulaga, H., Hillel, A., Ramanathan, M., Jr., and Lane, A.P. (2020). Elevated ACE-2 expression in the olfactory neuroepithelium: implications for anosmia and upper respiratory SARS-CoV-2 entry and replication. Eur. Respir. J. *56*, 2001948.

Daly, J.L., Simonetti, B., Klein, K., Chen, K.E., Williamson, M.K., Anton-Plagaro, C., Shoemark, D.K., Simon-Gracia, L., Bauer, M., Hollandi, R., et al. (2020). Neuropilin-1 is a host factor for SARS-CoV-2 infection. Science *370*, 861–865.

de Melo, G.D., Lazarini, F., Levallois, S., Hautefort, C., Michel, V., Larrous, F., Verillaud, B., Aparicio, C., Wagner, S., Gheusi, G., et al. (2021). COVID-19-related anosmia is associated with viral persistence and inflammation in human olfactory epithelium and brain infection in hamsters. Sci. Transl. Med. *13*, eabf8396.

Delsing, L., Donnes, P., Sanchez, J., Clausen, M., Voulgaris, D., Falk, A., Herland, A., Brolen, G., Zetterberg, H., Hicks, R., and Synnergren, J. (2018). Barrier properties and transcriptome expression in human iPSC-derived models of the blood-brain barrier. Stem Cells *36*, 1816–1827.

Desforges, M., Le Coupanec, A., Stodola, J.K., Meessen-Pinard, M., and Talbot, P.J. (2014). Human coronaviruses: viral and cellular factors involved in neuroinvasiveness and neuropathogenesis. Virus Res. *194*, 145–158.

Dinnon, K.H., 3rd, Leist, S.R., Schafer, A., Edwards, C.E., Martinez, D.R., Montgomery, S.A., West, A., Yount, B.L., Jr., Hou, Y.J., Adams, L.E., et al. (2020). A mouse-adapted model of SARS-CoV-2 to test COVID-19 countermeasures. Nature *586*, 560–566.

Dobin, A., Davis, C.A., Schlesinger, F., Drenkow, J., Zaleski, C., Jha, S., Batut, P., Chaisson, M., and Gingeras, T.R. (2013). STAR: ultrafast universal RNA-seq aligner. Bioinformatics *29*, 15–21.

Durinck, S., Spellman, P.T., Birney, E., and Huber, W. (2009). Mapping identifiers for the integration of genomic datasets with the R/Bioconductor package biomaRt. Nat. Protoc. *4*, 1184–1191.

Ellinger, B., Bojkova, D., Zaliani, A., Cinatl, J., Claussen, C., Westhaus, S., Keminer, O., Reinshagen, J., Kuzikov, M., Wolf, M., et al. (2021). A SARS-CoV-2 cytopathicity dataset generated by high-content screening of a large drug repurposing collection. Sci. Data *8*, 70.

Ellul, M.A., Benjamin, L., Singh, B., Lant, S., Michael, B.D., Easton, A., Kneen, R., Defres, S., Sejvar, J., and Solomon, T. (2020). Neurological associations of COVID-19. Lancet Neurol. *19*, 767–783.

Glowacka, I., Bertram, S., Herzog, P., Pfefferle, S., Steffen, I., Muench, M.O., Simmons, G., Hofmann, H., Kuri, T., Weber, F., et al. (2010). Differential downregulation of ACE2 by the spike proteins of severe acute respiratory syndrome coronavirus and human coronavirus NL63. J. Virol. *84*, 1198–1205.

Hawkins, B.T., and Davis, T.P. (2005). The blood-brain barrier/neurovascular unit in health and disease. Pharmacol. Rev. *57*, 173–185.

Helms, J., Kremer, S., Merdji, H., Clere-Jehl, R., Schenck, M., Kummerlen, C., Collange, O., Boulay, C., Fafi-Kremer, S., Ohana, M., et al. (2020). Neurologic features in severe SARS-CoV-2 infection. N. Engl. J. Med. *382*, 2268–2270.

Hoffmann, M., Kleine-Weber, H., Schroeder, S., Kruger, N., Herrler, T., Erichsen, S., Schiergens, T.S., Herrler, G., Wu, N.H., Nitsche, A., et al. (2020). SARS-CoV-2 cell entry depends on ACE2 and TMPRSS2 and is blocked by a clinically proven protease inhibitor. Cell *181*, 271–280.e8.

Hollmann, E.K., Bailey, A.K., Potharazu, A.V., Neely, M.D., Bowman, A.B., and Lippmann, E.S. (2017). Accelerated differentiation of human induced pluripotent stem cells to blood-brain barrier endothelial cells. Fluids Barriers CNS *14*, 9.

Iadecola, C., Anrather, J., and Kamel, H. (2020). Effects of COVID-19 on the nervous system. Cell *183*, 16–27.e11.

Kim, B.J., Bee, O.B., McDonagh, M.A., Stebbins, M.J., Palecek, S.P., Doran, K.S., and Shusta, E.V. (2017). Modeling group B Streptococcus and blood-brain barrier interaction by using induced pluripotent stem cell-derived brain endothelial cells. mSphere *2*, e00398-17.

Kim, B.J., and Schubert-Unkmeir, A. (2019). In vitro models for studying the interaction of Neisseria meningitidis with human brain endothelial cells. Methods Mol. Biol. *1969*, 135–148.

Liao, Y., Smyth, G.K., and Shi, W. (2014). featureCounts: an efficient general purpose program for assigning sequence reads to genomic features. Bioinformatics *30*, 923–930.

Lim, R.G., Quan, C., Reyes-Ortiz, A.M., Lutz, S.E., Kedaigle, A.J., Gipson, T.A., Wu, J., Vatine, G.D., Stocksdale, J., Casale, M.S., et al. (2017). Huntington's disease iPSC-derived brain microvascular endothelial cells reveal WNT-mediated angiogenic and blood-brain barrier deficits. Cell Rep. *19*, 1365–1377.

Lippmann, E.S., Al-Ahmad, A., Azarin, S.M., Palecek, S.P., and Shusta, E.V. (2014). A retinoic acid-enhanced, multicellular human blood-brain barrier model derived from stem cell sources. Sci. Rep. *4*, 4160.

Lippmann, E.S., Azarin, S.M., Kay, J.E., Nessler, R.A., Wilson, H.K., Al-Ahmad, A., Palecek, S.P., and Shusta, E.V. (2012). Derivation of

blood-brain barrier endothelial cells from human pluripotent stem cells. Nat. Biotechnol. *30*, 783–791.

Lippmann, E.S., Azarin, S.M., Palecek, S.P., and Shusta, E.V. (2020). Commentary on human pluripotent stem cell-based blood-brain barrier models. Fluids Barriers CNS *17*, 64.

Love, M.I., Huber, W., and Anders, S. (2014). Moderated estimation of fold change and dispersion for RNA-seq data with DESeq2. Genome Biol. *15*, 550.

Lu, T.M., Houghton, S., Magdeldin, T., Duran, J.G.B., Minotti, A.P., Snead, A., Sproul, A., Nguyen, D.T., Xiang, J., Fine, H.A., et al. (2021). Pluripotent stem cell-derived epithelium misidentified as brain microvascular endothelium requires ETS factors to acquire vascular fate. Proc. Natl. Acad. Sci. U S A *118*, e2016950118.

Mao, L., Jin, H., Wang, M., Hu, Y., Chen, S., He, Q., Chang, J., Hong, C., Zhou, Y., Wang, D., et al. (2020). Neurologic manifestations of hospitalized patients with coronavirus disease 2019 in Wuhan, China. JAMA Neurol. *77*, 683–690.

Martins Gomes, S.F., Westermann, A.J., Sauerwein, T., Hertlein, T., Forstner, K.U., Ohlsen, K., Metzger, M., Shusta, E.V., Kim, B.J., Appelt-Menzel, A., and Schubert-Unkmeir, A. (2019). Induced pluripotent stem cell-derived brain endothelial cells as a cellular model to study Neisseria meningitidis infection. Front. Microbiol. *10*, 1181.

Matschke, J., Lutgehetmann, M., Hagel, C., Sperhake, J.P., Schroder, A.S., Edler, C., Mushumba, H., Fitzek, A., Allweiss, L., Dandri, M., et al. (2020). Neuropathology of patients with COVID-19 in Germany: a post-mortem case series. Lancet Neurol. *19*, 919–929.

Meinhardt, J., Radke, J., Dittmayer, C., Franz, J., Thomas, C., Mothes, R., Laue, M., Schneider, J., Brunink, S., Greuel, S., et al. (2021). Olfactory transmucosal SARS-CoV-2 invasion as a port of central nervous system entry in individuals with COVID-19. Nat. Neurosci. *24*, 168–175.

Merico, D., Isserlin, R., Stueker, O., Emili, A., and Bader, G.D. (2010). Enrichment map: a network-based method for gene-set enrichment visualization and interpretation. PLoS One *5*, e13984.

Merritt, C.R., Ong, G.T., Church, S.E., Barker, K., Danaher, P., Geiss, G., Hoang, M., Jung, J., Liang, Y., McKay-Fleisch, J., et al. (2020). Multiplex digital spatial profiling of proteins and RNA in fixed tissue. Nat. Biotechnol. *38*, 586–599.

Monteil, V., Kwon, H., Prado, P., Hagelkruys, A., Wimmer, R.A., Stahl, M., Leopoldi, A., Garreta, E., Hurtado Del Pozo, C., Prosper, F., et al. (2020). Inhibition of SARS-CoV-2 infections in engineered human tissues using clinical-grade soluble human ACE2. Cell *181*, 905–913 e907.

Norz, D., Frontzek, A., Eigner, U., Oestereich, L., Wichmann, D., Kluge, S., Fischer, N., Aepfelbacher, M., Pfefferle, S., and Lutgehetmann, M. (2020). Pushing beyond specifications: evaluation of linearity and clinical performance of the cobas 6800/8800 SARS-CoV-2 RT-PCR assay for reliable quantification in blood and other materials outside recommendations. J. Clin. Virol. *132*, 104650.

Patel, R., Hossain, M.A., German, N., and Al-Ahmad, A.J. (2018). Gliotoxin penetrates and impairs the integrity of the human blood-brain barrier in vitro. Mycotoxin Res. *34*, 257–268.

Pei, R., Feng, J., Zhang, Y., Sun, H., Li, L., Yang, X., He, J., Xiao, S., Xiong, J., Lin, Y., et al. (2020). Host metabolism dysregulation and cell tropism identification in human airway and alveolar organoids upon SARS-CoV-2 infection. Protein Cell *12*, 717–733.

Pfefferle, S., Huang, J., Norz, D., Indenbirken, D., Lutgehetmann, M., Oestereich, L., Gunther, T., Grundhoff, A., Aepfelbacher, M., and Fischer, N. (2020a). Complete genome sequence of a SARS-CoV-2 strain isolated in Northern Germany. Microbiol. Resour. Announc. *9*, e00520-20.

Pfefferle, S., Reucher, S., Norz, D., and Lutgehetmann, M. (2020b). Evaluation of a quantitative RT-PCR assay for the detection of the emerging coronavirus SARS-CoV-2 using a high throughput system. Euro Surveill. *25*, 2000152.

Puelles, V.G., Lutgehetmann, M., Lindenmeyer, M.T., Sperhake, J.P., Wong, M.N., Allweiss, L., Chilla, S., Heinemann, A., Wanner, N., Liu, S., et al. (2020). Multiorgan and renal tropism of SARS-CoV-2. N. Engl. J. Med. *383*, 590–592.

Ramani, A., Muller, L., Ostermann, P.N., Gabriel, E., Abida-Islam, P., Muller-Schiffmann, A., Mariappan, A., Goureau, O., Gruell, H., Walker, A., et al. (2020). SARS-CoV-2 targets neurons of 3D human brain organoids. EMBO J. *39*, e106230.

Rhea, E.M., Logsdon, A.F., Hansen, K.M., Williams, L.M., Reed, M.J., Baumann, K.K., Holden, S.J., Raber, J., Banks, W.A., and Erickson, M.A. (2021). The S1 protein of SARS-CoV-2 crosses the blood-brain barrier in mice. Nat. Neurosci. *24*, 368–378.

Ritchie, M.E., Phipson, B., Wu, D., Hu, Y., Law, C.W., Shi, W., and Smyth, G.K. (2015). Limma powers differential expression analyses for RNA-sequencing and microarray studies. Nucleic Acids Res. *43*, e47.

Schwabenland, M., Salie, H., Tanevski, J., Killmer, S., Lago, M.S., Schlaak, A.E., Mayer, L., Matschke, J., Puschel, K., Fitzek, A., et al. (2021). Deep spatial profiling of human COVID-19 brains reveals neuroinflammation with distinct microanatomical microglia-T-cell interactions. Immunity *54*, 1594–1610.e11.

Shi, G., Kenney, A.D., Kudryashova, E., Zani, A., Zhang, L., Lai, K.K., Hall-Stoodley, L., Robinson, R.T., Kudryashov, D.S., Compton, A.A., and Yount, J.S. (2021). Opposing activities of IFITM proteins in SARS-CoV-2 infection. EMBO J. *40*, e106501.

Solomon, I.H., Normandin, E., Bhattacharyya, S., Mukerji, S.S., Keller, K., Ali, A.S., Adams, G., Hornick, J.L., Padera, R.F., Jr., and Sabeti, P. (2020). Neuropathological features of Covid-19. N. Engl. J. Med. *383*, 989–992.

Song, E., Zhang, C., Israelow, B., Lu-Culligan, A., Prado, A.V., Skriabine, S., Lu, P., Weizman, O.E., Liu, F., Dai, Y., et al. (2021). Neuroinvasion of SARS-CoV-2 in human and mouse brain. J. Exp. Med. *218*, e20202135.

Sun, S.H., Chen, Q., Gu, H.J., Yang, G., Wang, Y.X., Huang, X.Y., Liu, S.S., Zhang, N.N., Li, X.F., Xiong, R., et al. (2020). A mouse model of SARS-CoV-2 infection and pathogenesis. Cell Host Microbe *28*, 124–133.e4.

Tay, M.Z., Poh, C.M., Renia, L., MacAry, P.A., and Ng, L.F.P. (2020). The trinity of COVID-19: immunity, inflammation and intervention. Nat. Rev. Immunol. *20*, 363–374.

Vatine, G.D., Al-Ahmad, A., Barriga, B.K., Svendsen, S., Salim, A., Garcia, L., Garcia, V.J., Ho, R., Yucer, N., Qian, T., et al. (2017). Modeling psychomotor retardation using iPSCs from MCT8-deficient patients indicates a prominent role for the blood-brain barrier. Cell Stem Cell *20*, 831–843 e835.

Wenzel, J., Lampe, J., Muller-Fielitz, H., Schuster, R., Zille, M., Muller, K., Krohn, M., Korbelin, J., Zhang, L., Ozorhan, U., et al. (2021). The SARS-CoV-2 main protease M(pro) causes microvascular brain pathology by cleaving NEMO in brain endothelial cells. Nat. Neurosci. *24*, 1522–1533.

Woo, M.S., Malsy, J., Pottgen, J., Seddiq Zai, S., Ufer, F., Hadjilaou, A., Schmiedel, S., Addo, M.M., Gerloff, C., Heesen, C., et al. (2020). Frequent neurocognitive deficits after recovery from mild COVID-19. Brain Commun. *2*, fcaa205.

Yu, G., Wang, L.G., Han, Y., and He, Q.Y. (2012). clusterProfiler: an R package for comparing biological themes among gene clusters. OMICS *16*, 284–287.

Zimniak, M., Kirschner, L., Hilpert, H., Geiger, N., Danov, O., Oberwinkler, H., Steinke, M., Sewald, K., Seibel, J., and Bodem, J. (2021). The serotonin reuptake inhibitor Fluoxetine inhibits SARS-CoV-2 in human lung tissue. Sci. Rep. *11*, 5890.

Stem Cell Reports, Volume *17*

Supplemental Information

The blood-brain barrier is dysregulated in COVID-19 and serves as a CNS entry route for SARS-CoV-2

Susanne Krasemann, Undine Haferkamp, Susanne Pfefferle, Marcel S. Woo, Fabian Heinrich, Michaela Schweizer, Antje Appelt-Menzel, Alevtina Cubukova, Janica Barenberg, Jennifer Leu, Kristin Hartmann, Edda Thies, Jessica Lisa Littau, Diego Sepulveda-Falla, Liang Zhang, Kathy Ton, Yan Liang, Jakob Matschke, Franz Ricklefs, Thomas Sauvigny, Jan Sperhake, Antonia Fitzek, Anna Gerhartl, Andreas Brachner, Nina Geiger, Eva-Maria König, Jochen Bodem, Sören Franzenburg, Andre Franke, Stefan Moese, Franz-Josef Müller, Gerd Geisslinger, Carsten Claussen, Aimo Kannt, Andrea Zaliani, Philip Gribbon, Benjamin Ondruschka, Winfried Neuhaus, Manuel A. Friese, Markus Glatzel, and Ole Pless

Supplemental information

Supplemental figures and legends

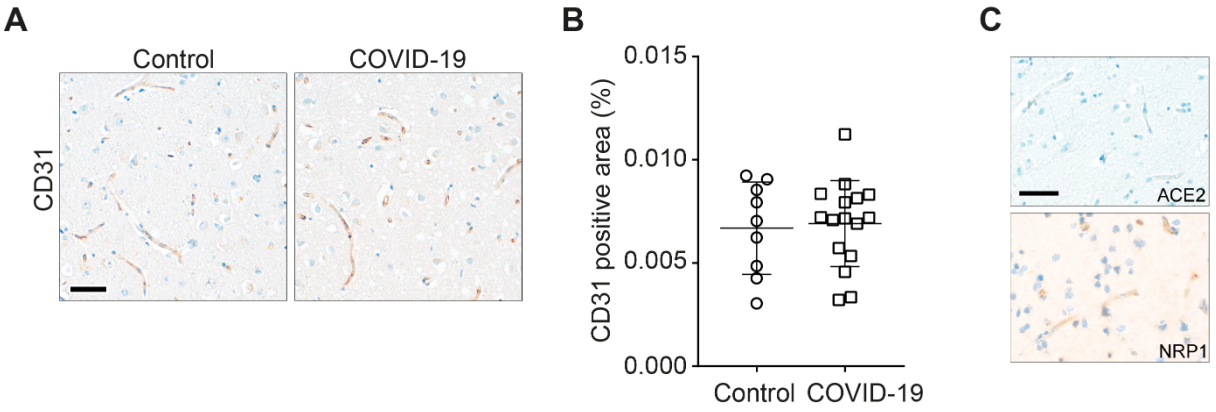

SI Figure 1: Expression of CD31 is not altered in COVID-19 brains and control brains express ACE2 and NRP1 in the vasculature. (A) Representative images of immune-histochemical staining for CD31 (brown) in control or COVID-19 human cortex brain tissue. No differences in expression can be observed. Scale bar: 50 μM. **(B)** Quantification of the signal as in (A) of CD31-positive area (%) in COVID-19 vs. control cortex tissue confirmed that CD31 expression is not altered in fatal SARS-CoV-2 infection. **(C)** Representative images of ACE2 and NRP1 expression in human cortex brain tissue. Scale bar: 50 μm.

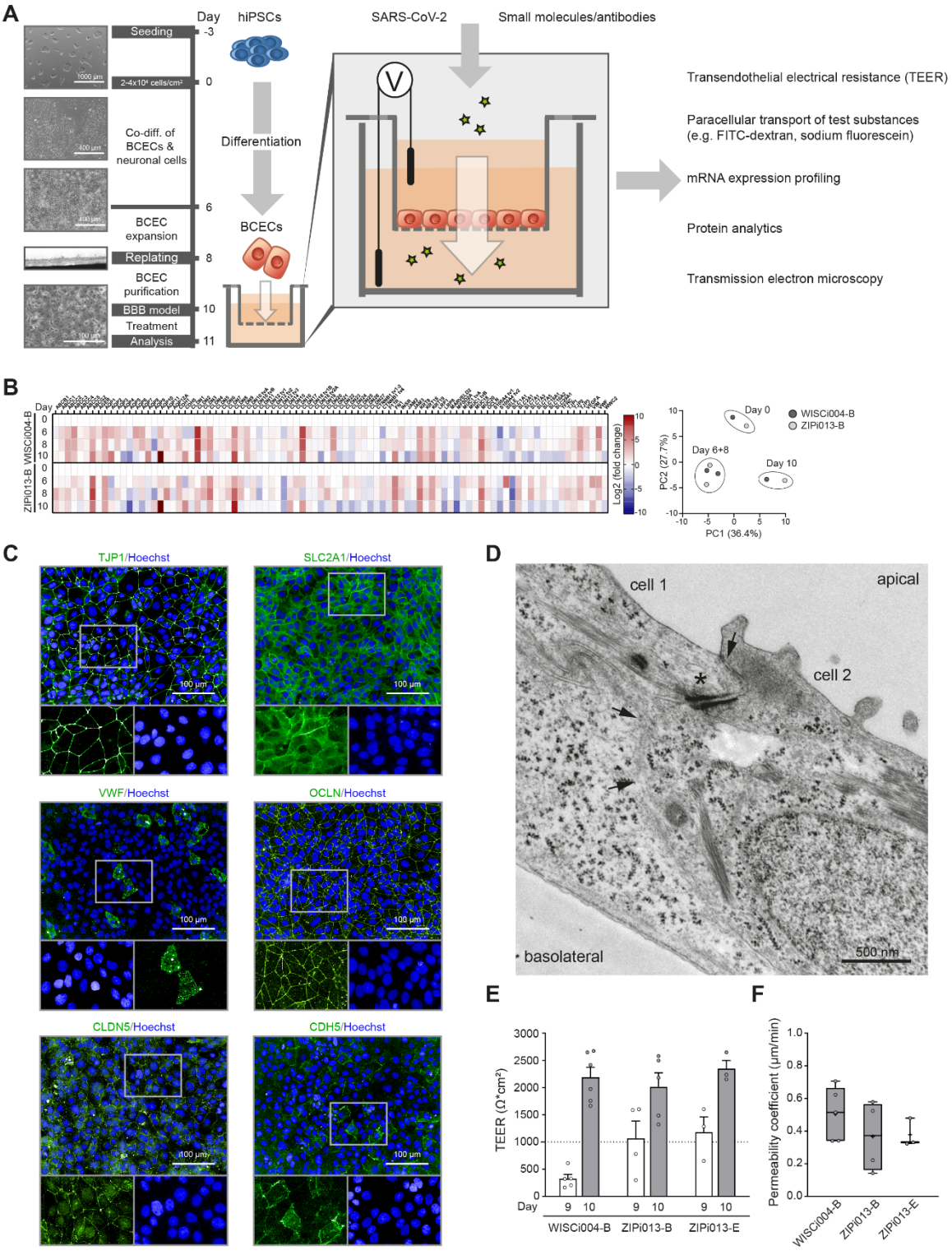

SI Figure 2: hiPS-derived brain capillary endothelial-like cell transwell model. (A) Schematic representation of the transwell model. After 10 days of differentiation, the size of hiPS-BCECs was increased compared to the donor hiPSCs and cells grew in close contact forming a confluent monolayer. **(B)** Expression of key BCEC marker genes during the course of differentiation, in particular tight junction (TJ) proteins (claudins, occludin), junction adhesion molecules (JAMs), adherence junction (AJ) proteins, solute carriers and efflux transporters. hiPS-BCECs derived from hiPSC lines WISCi004-B or ZIPi013-B show an increased expression of several of these transcripts. Respective time points are plotted (d=6, d=8, d=10) and were normalized to the respective hiPSC donor lines. In principle component analysis (PCA) the samples cluster according to the differentiation stage, indicating the

robustness of the differentiation protocol. **(C)** Expression of BCEC-specific marker proteins (TJP1, SLC2A1, VWF, OCLN, CLDN5, CDH5) after day 10 of the differentiation procedure (green). Nuclei stained with Hoechst 33258 (blue). Scale bars as indicated. **(D)** Transmission electron microscopy images of hiPS-BCECs. Neighboring cells are connected by complex TJs constricting the paracellular space (black arrows). Furthermore, adhesion points (punctum adherens, black asterisk in d) anchored within the actin filament network were detected, indicating the integrity of cell-cell contacts. Scale bars as indicated. **(E)** At day 9, TEER values were ~300 $\Omega*cm^2$, but at day 10 increased drastically to values of ~2000 $\Omega*cm^2$, a typical increase in barrier integrity and formation of associated TJ structures around that time. For all experiments of this study, only inserts with TEER values > 1000 $\Omega*cm^2$ were considered. Mean ± SEM of at least three independent biological experiments, at least three technical replicates each. **(F)** To characterize the size-dependent paracellular permeability of the BBB models, which is functionally linked to the expression of junctional molecules, especially of claudins, transport studies with the paracellular marker fluorescein (~0.33 kDa) were conducted. Fluorescein permeated very similarly in BBB models derived from three independent hiPSC lines (WISCi004-B, ZIPi013-B, ZIPi013-E). Mean ± SEM of at least three independent biological experiments, at least three technical replicates each.

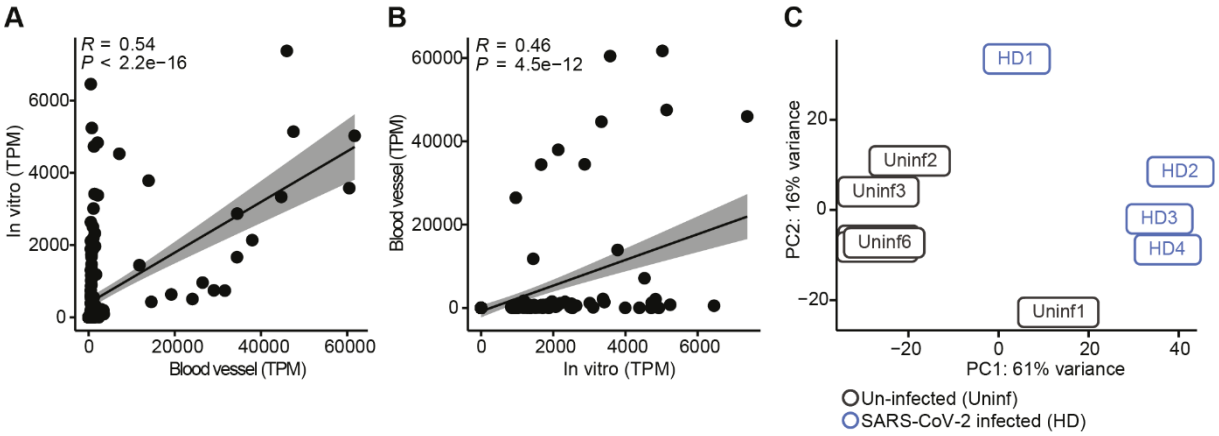

SI Figure 3: Transcriptional correlation of human cortical blood vessels with hiPS-BCECs. (A) Correlation of highest 100 and lowest 100 genes of hiPS-BCECs with respective genes in human cortical blood vessels. Normally distributed Pearson correlation was used. $R = 0.54$, $P < 2.2e\text{-}16$. **(B)** Correlation of highest 100 and lowest 100 genes of human blood vessels with respective genes in hiPS-BCECs. Normally distributed Pearson correlation was used. $R = 0.46$, $P = 4.5e\text{-}12$. **(C)** Principal component analysis of un-infected (n = 6) and SARS-CoV-2 infected hiPS-BCECs (n = 4). TPM: Transcripts per million.

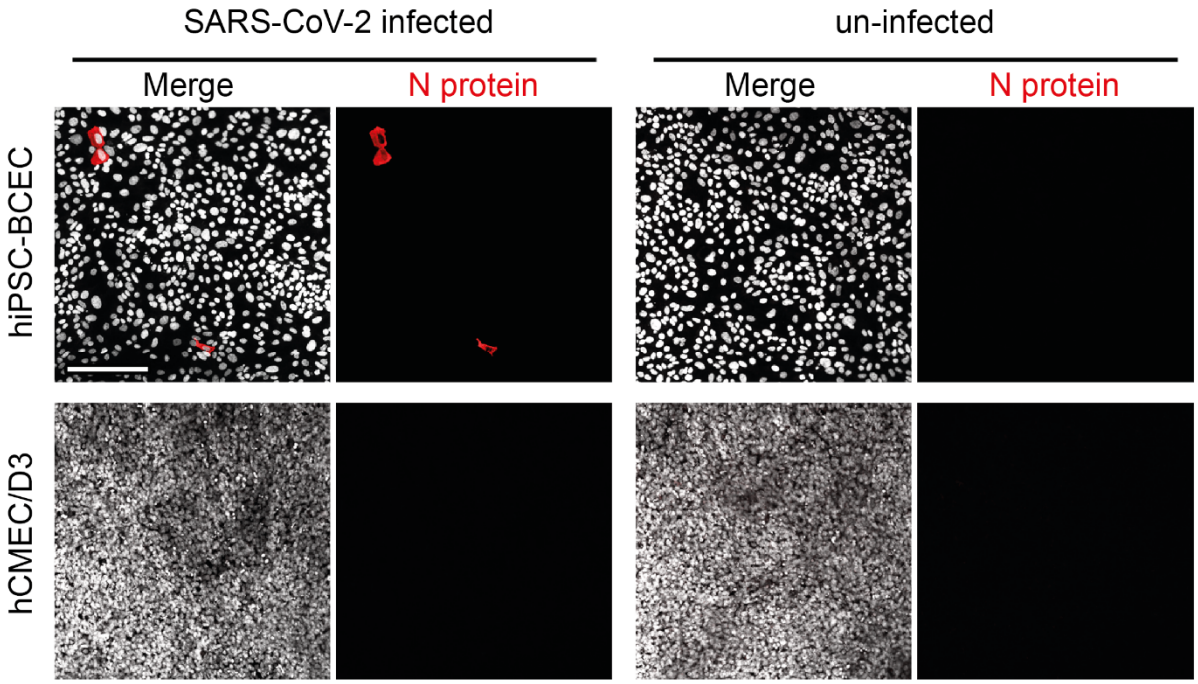

SI Figure 4: SARS-CoV-2 infection of hiPSC-BCECs and hCMEC/D3 in parallel. **Top row**: Representative images of infected/un-infected hiPSC-BCECs differentiated from WISCi004-B (IMR90-4). SARS-CoV-2 N protein staining (red), nuclei stained with DAPI (white). **Bottom row**: Representative images of infected/un-infected hCMEC/D3. SARS-CoV-2 N protein staining (red), nuclei stained with DAPI (white). Despite higher cell counts, not a single SARS-CoV-2 N protein positive hCMEC/D3 cell was observed after inf ection with an MOI of 10 in 4 independent wells (area 21.6 x 11.4 mm^2 each). Scale bar: 200 µm.

Supplemental table

SI Table 1: Epidemiological and clinical features of COVID-19 patients and controls.

Age (years)	Sex	Body mass index, kg/m^2	Place of death	Post mortem interval (days)	Disease course (days)	Cause of death	SARS-CoV-2 qPCR (brain)	Comorbidities	Mechanical ventilation
76 #	m	37.7	Intensive care unit	3	23	Sepsis	+	Adipositas, AML, DCM, S/P thyroid cancer	y
86 #	f	30.5	Hospital ward	3	10	Pneumonia	n.d.	Adipositas, atrial fibrillation, CHD, CKD, dementia, myelodysplastic syndrome	n
67 #	m	33.5	Hospital ward	2	2	Pneumonia, circulating distrubances in inflammation	n.d.	Adipositas, AH, DCM, lung emphysema, PD, schizophrenia, Type II diabetes	n
66	m	25.3	Emergency room	2	n.d.	Pneumonia	+	CHD, Type II diabetes	n
82	f	15.4	Hospital ward	4	5	Bronchitis	+	COPD, CKD, S/P PE	n
77	m	19.4	Hospital ward	2	29	Pneumonia	+	Atrial fibrillation, aortic aneurysm, cardiac hypertrophy, CKD, lung emphysema	n
85 #	f	18.1	Hospital ward	0	20	Pneumonia	+	Atrial fibrillation, cardiac insufficiency, CHD, CKD, myelofibrosis	n
51	m	20.7	Home	8	P. m. diagnosis	Pneumonia	n.d.	Liver cirrhosis	n
87	f	16.4	Hospital ward	3	2	Pneumonia, sepsis	n.d.	Colon cancer, emphysema, paranoid schizophrenia	n
76	f	21.7	Hospital ward	2	6	Pneumonia	n.d.	AH, breast cancer	n
59	f	ND	Intensive care unit	1	18	Pneumonia	+	Multiple myeloma	y
78 #	m	25.5	Home	2	P.m. diagnosis	Myocardial infarction	n.d.	AH, cardiac insufficiency, CHD, emphysema, liver cirrhosis	n
89 #	f	17.8	Hospital ward	2	1	Pneumonia	n.d.	Atrial fibrillation, CHD, S/P myocardial infarction	n

29 #	m	25.5	Work	6	2	Bronchopneumonia	n.d.	Cardiac hypertrophy, steatosis hepatis	n
46 #	f	n.d.	Home	1	No COVID-19	Myocardial infarction	-	n.d.	n
79	m	n.d.	n.d.	3	No COVID-19	Septic shock	-	n.d.	n
90	f	n.d.	n.d.	8	No COVID-19	Haemorrhagic shock	-	n.d.	n
92	m	n.d.	n.d.	13	No COVID-19	Heart failure	-	n.d.	n
66 #	f	n.d.	n.a.	Biopsy	No COVID-19	n.a.	-	Surgery for temporal lobe epilepsy	n
70 §	f	n.d.	n.a.	Biopsy	No COVID-19	n.a.	-	Surgery for temporal lobe epilepsy	n
62 #	m	n.d.	n.a.	Biopsy	No COVID-19	n.a.	-	Surgery for temporal lobe epilepsy	n
47 #	m	n.d.	n.a.	Biopsy	No COVID-19	n.a.	-	Surgery for temporal lobe epilepsy	n
37 §	m	n.d.	n.a.	Biopsy	No COVID-19	n.a.	-	Surgery for temporal lobe epilepsy	n
65 # §	f	n.d.	n.a.	Biopsy	No COVID-19	n.a.	-	Surgery for temporal lobe epilepsy	n

Abbreviations: m, male; f, female; AML, acute myeloleukaemia; DCM, dilated cardiomyopathy; S/P, status post; CHD, coronary heart disease; CKD, chronic kidney disease; AH, arterial hypertension; PD, Parkinson's Disease; COPD, chronic obstructive pulmonary disease; PE, pulmonary embolism; y, yes; n, no; # samples used for Nanostring DSP; § samples used for vessel isolation and RNA-seq; n.d. not determined; n.a. not applicable

Supplemental experimental procedures

Human induced pluripotent stem cells

We maintained human iPSCs lines WISCi004-B (Kadari et al., 2014), ZIPi013-B and ZIPi013-E (Tandon et al., 2018) in mTeSR™1 (#05850, mTeSR™1 Complete Kit, STEMCELL Technologies) under feeder-free conditions on Matrigel™ (Corning) coated multiwell plates at 37 °C with 5% CO_2. Cells were passaged at 70-80% confluency via incubation with Gentle Cell Dissociation Reagent (#07174, STEMCELL Technologies,) for 7 min at room temperature. Gentle Cell Dissociation Reagent was aspired, 1 ml mTeSR™1 was added and colonies were detached by scraping with a cell scraper. Cell aggregates were pipetted up and down in order to dissociate the colonies and seeded in fresh mTeSR™1 onto newly Matrigel™-coated plates in a 1:10-1:60 split ratio. Medium was exchanged on a daily basis.

hiPS-BCEC differentiation and establishment of the *in vitro* BBB model

For the infection model, we used the hiPSC line WISCi004-B/IMR90-4 (Kadari et al., 2014), but have also validated the model using hiPSC lines ZIPi013-B and ZIPi013-E (Tandon et al., 2018). WISCi004-B was extensively characterized by staining and quantifying pluripotency-associated markers, including OCT3/4, NANOG, SOX-2, LIN28 and CMYC, ScoreCard (Bock et al., 2011; Tsankov et al., 2015) and PluriTest analysis (Muller et al., 2011), which all passed. Initially, a single cell suspension of hiPSCs was prepared with Accutase (#A1110501, ThermoFisher Scientific). The cell suspension was centrifuged at 300 x g for 5 min and cells were seeded in mTeSR™1 supplemented with 10 µM Y-27632 (#72304, STEMCELL Technologies) onto Matrigel-coated 6-well plates (Nunc™, #140675, ThermoFisher Scientific). The seeding density was optimized for each hiPSC line. For the differentiation of hiPSCs to BCECs, the neurodevelopmental process *in vivo* has to be recapitulated *in vitro*. For brain-capillary endothelial-like cells, a co-differentiation of neural and endothelial cells was initiated by treatment with so-called unconditioned medium (Lippmann et al., 2014). After 2-3 days

when optimal cell densities of 2-4x10^4 cells/cm^2 were reached, medium was switched to unconditioned medium in order to initiate co-differentiation of BCECs and neuronal cells (referred to as day 0 of differentiation throughout the manuscript). Unconditioned medium was composed of 78.5% DMEM/F12 (#21331046, ThermoFisher Scientific), 20% KnockOut™ serum replacement (#10828028, ThermoFisher Scientific), 1% MEM NEAA (#1114050, ThermoFisher Scientific), 0.5% L-glutamine (#GLN-B, Capricorn), and 0.1 mM β-mercaptoethanol (#21985023, ThermoFisher Scientific). A daily change of unconditioned medium for 5 days was followed by double feeding at day 6 with endothelial cell (EC) medium supplemented with 20 ng/ml hbFGF (#D100-18B, Peprotech) and 10 µM retinoic acid (RA, #722262, STEMCELL Technologies) to expand the BCECs. EC medium was composed of Human Endothelial-SFM (#11111044, ThermoFisher Scientific) and, if not stated otherwise, 0.5% B27 Supplement (#17504044, ThermoFisher Scientific) as described recently (Neal et al., 2019). After 48 h without medium change, cells were dissociated with Accutase for 30 min and seeded at a cell density of 1x10^6 cells/cm^2 onto collagen IV/fibronectin-coated transwell inserts (#662-641, Greiner) in EC medium supplemented with 20 ng/mL hFGF and 10 µM RA. This seeding step at day 8 in combination with the collagen IV/fibronectin-coating allows for an efficient purification of BCECs. At day 9, hiPS-BCECs were adapted to EC medium without hFGF and RA (in transwell systems with 200 µl of medium apical and 800 µl basolateral) for 24 h. TEER measurements were performed to evaluate the integrity of the generated *in vitro* BBB to be used for further applications.

cDNA synthesis and low-volume qPCR for hiPS-BCEC characterization

These experiments were conducted as described previously (Ramme et al., 2019). For high-throughput qPCR, cells were harvested and total RNA was extracted according to the manufacturer's instructions using the NucleoSpin® RNA Kit (#740955.250, Macherey-Nagel). RNA concentration and quality was determined using a NanoDrop™ 1000 Spectrophotometer (ThermoFisher Scientific) and samples were stored at -80 °C until further use. A total volume

of 20 µl cDNA was synthesized from 250 ng of RNA using the High Capacity cDNA Reverse Transcriptase Kit (#4368814, Thermo Fisher Scientific). Targets were preamplified in order to increase the concentration of the targets and reduce required input sample volume. For preamplification the tenfold concentration of gene targeting primers was used in combination with Qiagen Mastermix and HotStar Plus Taq Polymerase (#203603, Qiagen). The high-throughput qPCR was performed with the preamplified cDNA in 96 samples × 96 targets chips using the Biomark™ System (Fluidigm®). The following 90 targets were investigated (claudin nomenclature according to (Mineta et al., 2011)): *ABCB1*, *ABCC1*, *ABCC2*, *ABCC3*, *ABCC4*, *ABCC5*, *ABCG2*, *AGER*, *AQP1*, *AQP2*, *AQP3*, *AQP4*, *AQP5*, *AQP6*, *AQP7*, *AQP8*, *AQP9*, *AQP10*, *AQP11*, *AQP12A*, *CDH1*, *CDH5*, *CLDN1*, *CLDN2*, *CLDN3*, *CLDN4*, *CLDN5*, *CLDN6*, *CLDN7*, *CLDN8*, *CLDN9*, *CLDN10 tva*, *CLDN10 tvb*, *CLDN11*, *CLDN12 tv1*, *CLDN12 tv2*, *CLDN12 tv3*, *CLDN14*, *CLDN15*, *CLDN16*, *CLDN17*, *CLDN18 tv1b*, *CLDN18 tv2a*, *CLDN19*, *CLDN20*, *CLDN21*, *CLDN22*, *CLDN23*, *CLDN24*, *CLDN25, CLDN26*, *CLDN27*, *CTNNB1 tv1-3*, *CTNNB1 tv4*, *F11R*, *FN1*, *INSR*, *JAM2*, *JAM3*, *KRT8*, *KRT18*, *KRT19*, *LRP1*, *LRP8*, *MARVELD2*, *MFSD2A*, *MUC1 tva*, *MUC1 tvb*, *MUC18*, *MUC20*, *OCLN*, *S100A4 tv1*, *S100A4 tv2*, *SELE*, *SLC1A1*, *SLC2A1*, *SLC7A1*, *SLC7A3*, *SLC7A5*, *SLC16A1*, *SLC16A2*, *SLC29A1*, *TFRC*, *TJP1*, *TJP2*, *TJP3*, *VEGFA*, *VIM*, *VWF*, *WWC2*. Threshold cycle (C_t) values were normalized to the endogenous housekeeping genes *PPIA*, *ACTB*, *GAPDH* and *B2M* and relative quantification was performed based on the comparative $2^{-\Delta Ct}$ method. Differential gene expression was visualized in a heatmap of the $\log_2$-fold change normalized to the respective hiPSC donor lines or with the two principle components obtained from PCA, which explain most of total variance.

Immunofluorescent staining of the SARS-CoV-2-infected or un-infected hiPS-BCEC monolayer and image analysis

hiPSC-derived BCECs were grown in 96-well imaging plates (#655-866, Greiner) or on transwell inserts (#662-641, Greiner) and fixed for 10 min in 4% formaldehyde. SARS-CoV-2

infected BCECs were soaked in formalin for 24 h. After washing with PBS, cells were permeabilized with 0.1-0.2% Triton X-100 in PBS. After additional washing, cells were blocked with 3% BSA and 0.1% Tween 20 in PBS or Blocking Medium (#15252, Active Motif). Primary antibodies were diluted in blocking solution and incubated overnight at 4 °C. The following antibodies and dilutions were applied: anti-TJP1/ZO-1 (1:400, #21773-1-AP, Proteintech), anti-SLC2A1/GLUT-1 (1:200, #ab115730, Abcam), anti-VWF (1:50, #555849, BD Pharmingen), anti-OCLN (1:200, #33-1500, ThermoFisher Scientific), anti-CLDN5 (1:100, #ab15106, Abcam), anti-CDH5 (1:100, # sc-9989, Santa Cruz Biotechnology), anti-spike (1:300; #GTX632604, GeneTex), anti-N (1:1000; #40143-T62, Sino Biological or 1:1000; #HS-452011, Synaptic Systems) and anti-dsRNA (1:200; #Ab01299-23.0; absolute antibody; rabbit monoclonal antibody of J2-anti-dsRNA antibody). Cells were thoroughly washed and then incubated with secondary antibodies (1:500, Alexa Fluor® 488/555/647 antibodies, ThermoFisher Scientific) diluted in blocking solution for 1-1.5 h at room temperature in the dark. Cells were then washed twice with PBS and nuclear counterstaining was performed for 15 min with 1 µg/ml Hoechst 33258 (#H3569, Invitrogen) or DAPI (#10184322, ThermoFisher Scientific), followed by two additional washing steps. Cells on 96-well imaging plates were imaged using the Opera or Operetta High Content Imaging System (PerkinElmer). The image analysis and quantification of the pluripotency-associated markers was performed using the Columbus™ Image Data Storage and Analysis system (PerkinElmer). Transwell insert membranes were carefully cut out and mounted upside down on glass slides (ibidi µ-Slide #80287) for confocal microscopy. These were imaged with a Leica SP5 confocal microscope and a 20x oil or 63x oil objective. Three random pictures were acquired with a size of 600,000 μm^2 per condition. 20x images were processed by ImageJ to determine the number of SARS-CoV-2 protein positive cells in relation to all DAPI-positive nuclei.

Fluorescein transport

Permeation of fluorescein across the established *in vitro* BBB model was measured to study the paracellular transport capacity and thus the tightness of the BBB. Fluorescein sodium salt (#F6377, Sigma-Aldrich) was dissolved in EC medium to a final concentration of 10 µM. The apical medium from all transwell inserts to be examined, including inserts containing cells (BBB model) and empty inserts (blanks), was replaced by 200 µl fluorescein solution. Immediately after, the inserts were transferred to a new 24-well plate containing 800 µl of fresh EC medium and placed for 1 h in the incubator at 37 °C and 5% CO_2. To assess fluorescence intensity, samples from both, apical and basolateral compartments, the 10 µM fluorescein starting solution and pure EC medium were pipetted into a 96-well plate (#655-900, Greiner). The concentration of the fluorescent tracer molecule in each sample was measured using a fluorescence plate reader (Infinite M1000 Pro, TECAN, excitation: 490 nm, emission: 525 nm) and the permeability coefficients were calculated as described previously (Neuhaus et al., 2008). In case of SARS-CoV-2 infection experiments, samples were mixed 1:1 with a buffer containing ≤ 40% guanidinie hydrochloride in Tris-HCl (Roche media kit, Roche) for inactivation prior to fluorescence intensity measurements.

Transendothelial electrical resistance (TEER) measurements

To evaluate the tightness and integrity of the generated *in vitro* BBB, the TEER across the hiPS-BCEC monolayer was measured in real-time without damaging the cells. To this end, alternating electrical signals were applied using electrodes placed on both sides of monolayer and the resulting voltage and current are used to calculate the electrical resistance in $\Omega*cm^2$. TEER values were measured using the Millicell®-ER system (#MERS00002, Merck Millipore) in combination with the STX01 electrode (Merck Millipore). Prior to the measurement, the electrode was placed in 70% ethanol for 10 min, then dipped into sterile H_2O and equilibrated in EC medium for at least 15 min. A test electrode (#STX04, Merck Millipore) was used to control and adjust the TEER instrument if necessary. The TEER measurements were performed 40 min after medium exchange. The 24-well plates containing the transwell inserts

were placed on an aluminium spacer plate positioned on a heating plate set to 37 °C and subsequently, the resistance was measured in both empty (blank) and cell containing inserts (BBB model) at three different positions of the insert membrane. TEER values were calculated based on the following formula:

$$TEER\ [\Omega * cm^2] = (R_{BBB\ model} - R_{blank})\ [\Omega] * A\ [cm^2]$$

R = resistance

A = culture area of the transwell insert

Transmission electron microscopy (TEM)

hiPS-BCECs were fixed with 1% glutaraldehyde and 4% paraformaldehyde in 0.1 M PBS, pH 7.2 overnight. Cells were washed three times with PBS, rinsed three times in 0.1 M sodium cacodylate buffer (pH 7.2-7.4) and osmicated using 1% osmium tetroxide in cacodylate buffer. Following osmication, the sections were dehydrated using ascending ethyl alcohol concentration steps, followed by two rinses in propylene oxide. Infiltration of the embedding medium was performed by immersing the samples in a 1:1 mixture of propylene oxide and Epon and finally in neat Epon. Polymerization was carried out at 60 °C. Semithin sections (0.5 µm) of cross-sections of hiPS-BCEC transwell cultures were prepared for light microscopy by staining for 1 minute with 1% Toluidine blue and mounting on glass slides. Ultrathin sections (60 nm) were examined in an EM902 (Zeiss). Pictures were acquired with a TRS 2K digital camera (A. Tröndle).

Isolation of human brain vessels

Human brain vessels were isolated as previously described (Lee et al., 2019). Briefly, fresh cortex tissue from a brain biopsy was homogenized in 1 ml MCDB131 medium (ThermoFischer Scientific) using a dounce homogenizer, further diluted in medium, and centrifuged (4 °C) at

2000 g for 5 min. The pellet was resuspended in 15% (wt/vol) 70 kDa dextran and centrifuged (4 °C) for 15 min at 10000 g. The microvessel containing pellet was retrieved and transferred to a 40 µm cell strainer. After washing with PBS, the microvessels were placed in 0.5% BSA/MCDB131 medium and centrifuged (4 °C) for 10 min at 5000 g. The final pellet was resolved in RNA isolation buffer and stored at -80 °C for further applications.

Immunohistochemical staining and analysis of human cortex tissue

Brain tissue was fixed in 4% buffered formalin and processed for paraffin embedding. Sections were cut (2 µm) and mounted. After dewaxing and inactivation of endogenous peroxidases (3% hydrogen peroxide), antibody-specific antigen retrieval was performed. Antibodies used in our study were anti-ACE2 (1:100; #AF933; R&D Systems), anti-NRP1 (1:500; #MBS178289, MyBiosource), anti-IFITM2 (1:3000; #MA5-27503, Invitrogen) and anti-CD31/PECAM1 (1:50; #HPA004690; Atlas Antibodies). Immunohistochemical staining were performed using a Ventana benchmark XT autostainer (Ventana). For detection of specific binding, the Ultra View Universal DAB Detection Kit (Ventana, Roche) was used which contains secondary antibodies, DAB stain, and counterstaining reagent for detection of nuclei. Slides were examined by experienced morphologists and representative pictures were taken with a Leica DMD108 digital microscope. For the quantification of specific signal, stained human cortex sections were scanned using a Hamamatsu NanoZoomer automatic digital slide scanner (Hamamatsu Photonics, Hamamatsu, Japan) and images of whole stained sections were obtained at a resolution of at least 1 pixel per µm. CD31 signals were assessed using ImageJ Software (version 1.52p, NIH, Bethesda, MA, USA). The plugin “colour deconvolution” and the H&E vectors were used to separate the channels (Ruifrok and Johnston, 2001). The brown channel with the RGB values (R: 0.26814753, G: 0.57031375, B: 0.77642715) was used. After applying the automatic threshold, the “analyze particles” script was used to measure the CD31 signal. Measurements included the area, standard deviation, min and max grey value, mean grey

value, shape descriptions and integrated density. The signal of the total tissue was measured to derive a portion of area covered by CD31.

hCMEC/D3 cultivation

hCMEC/D3 were cultured according to published protocols (Forster et al., 2008).

PluriTest analysis

For PluriTest analysis, RNA was isolated using the RNeasy Mini Kit (#74104, Qiagen) with an optional on-column DNase Digestion step (RNase-Free DNase Set, #79254, Qiagen). For microarray analysis, 200-500 ng of total RNA were amplified and biotinylated using the TargetAmp™ - Nano Labeling Kit for Illumina® Expression BeadChip (#TAN07924, Illumina). Concentration of Biotin-aRNA was measured with a Qubit 3.0 Fluorometer (Thermo Fisher Scientific) and the concentration of each sample was adjusted to 150 ng/µl. 750 ng of Biotin-aRNA were used for hybridization with the HumanHT-12 v4.0 Expression BeadChip (#BD-103-0604, Illumina) and hybridization was performed at 58 °C for 16-20 h. After hybridization, BeadChips were washed and stained according to the manufacturer's standard protocol. BeadChips were scanned using the iScan instrument (Illumina). Raw data (*.idat files) were submitted to PluriTest analysis at www.pluritest.org (Muller et al., 2011).

ScoreCard

ScoreCard assays were performed following the procedures outlined in the original publication (Tsankov et al., 2015).

Supplemental references

Bock, C., Kiskinis, E., Verstappen, G., Gu, H., Boulting, G., Smith, Z.D., Ziller, M., Croft, G.F., Amoroso, M.W., Oakley, D.H., et al. (2011). Reference Maps of human ES and iPS cell variation enable high-throughput characterization of pluripotent cell lines. Cell *144*, 439-452.

Forster, C., Burek, M., Romero, I.A., Weksler, B., Couraud, P.O., and Drenckhahn, D. (2008). Differential effects of hydrocortisone and TNFalpha on tight junction proteins in an in vitro model of the human blood-brain barrier. J Physiol *586*, 1937-1949.

Kadari, A., Lu, M., Li, M., Sekaran, T., Thummer, R.P., Guyette, N., Chu, V., and Edenhofer, F. (2014). Excision of viral reprogramming cassettes by Cre protein transduction enables rapid, robust and efficient derivation of transgene-free human induced pluripotent stem cells. Stem Cell Res Ther *5*, 47.

Lee, Y.K., Uchida, H., Smith, H., Ito, A., and Sanchez, T. (2019). The isolation and molecular characterization of cerebral microvessels. Nat Protoc *14*, 3059-3081.

Lippmann, E.S., Al-Ahmad, A., Azarin, S.M., Palecek, S.P., and Shusta, E.V. (2014). A retinoic acid-enhanced, multicellular human blood-brain barrier model derived from stem cell sources. Sci Rep *4*, 4160.

Mineta, K., Yamamoto, Y., Yamazaki, Y., Tanaka, H., Tada, Y., Saito, K., Tamura, A., Igarashi, M., Endo, T., Takeuchi, K., and Tsukita, S. (2011). Predicted expansion of the claudin multigene family. FEBS Lett *585*, 606-612.

Muller, F.J., Schuldt, B.M., Williams, R., Mason, D., Altun, G., Papapetrou, E.P., Danner, S., Goldmann, J.E., Herbst, A., Schmidt, N.O., et al. (2011). A bioinformatic assay for pluripotency in human cells. Nat Methods *8*, 315-317.

Neal, E.H., Marinelli, N.A., Shi, Y., McClatchey, P.M., Balotin, K.M., Gullett, D.R., Hagerla, K.A., Bowman, A.B., Ess, K.C., Wikswo, J.P., and Lippmann, E.S. (2019). A Simplified, Fully Defined Differentiation Scheme for Producing Blood-Brain Barrier Endothelial Cells from Human iPSCs. Stem Cell Reports *12*, 1380-1388.

Neuhaus, W., Plattner, V.E., Wirth, M., Germann, B., Lachmann, B., Gabor, F., and Noe, C.R. (2008). Validation of in vitro cell culture models of the blood-brain barrier: tightness characterization of two promising cell lines. J Pharm Sci *97*, 5158-5175.

Ramme, A.P., Koenig, L., Hasenberg, T., Schwenk, C., Magauer, C., Faust, D., Lorenz, A.K., Krebs, A.C., Drewell, C., Schirrmann, K., et al. (2019). Autologous induced pluripotent stem cell-derived four-organ-chip. Future Sci OA *5*, FSO413.

Ruifrok, A.C., and Johnston, D.A. (2001). Quantification of histochemical staining by color deconvolution. Anal Quant Cytol Histol *23*, 291-299.

Tandon, R., Brandl, B., Baryshnikova, N., Landshammer, A., Steenpass, L., Keminer, O., Pless, O., and Muller, F.J. (2018). Generation of two human isogenic iPSC lines from fetal dermal fibroblasts. Stem Cell Res *33*, 120-124.

Tsankov, A.M., Akopian, V., Pop, R., Chetty, S., Gifford, C.A., Daheron, L., Tsankova, N.M., and Meissner, A. (2015). A qPCR ScoreCard quantifies the differentiation potential of human pluripotent stem cells. Nat Biotechnol *33*, 1182-1192.